FURTHER PROBING THE MECHANISMS DRIVING REGIONAL PROJECTIONS OF EXTREME PRECIPITATION INTENSITY

MSAWENKOSI AGGRIPA THABO MPANZA

A THESIS SUBMITTED TO
THE FACULTY OF GRADUATE STUDIES
IN PARTIAL FULFILLMENT OF THE REQUIREMENTS
FOR THE DEGREE OF
MASTER OF SCIENCE

GRADUATE PROGRAM IN EARTH AND SPACE SCIENCE

YORK UNIVERSITY

TORONTO, ONTARIO

DECEMBER 2020

Abstract

Regional projections of extreme precipitation intensity (EPI) are strongly influenced by regional projections of “extreme ascent,”. Earlier studies are suggesting that long-term changes in eddy length and vertical stability are key factors influencing extreme ascent projections. We performed controlled experiments using the System for Atmospheric Modeling (SAM). Domains we chosen in the subtropical South Atlantic, where the Canadian Earth System Model version 2 (CanESM2) projects weakening of extreme ascent. SAM was forced with large-scale temperature, moisture and winds from CanESM2 during extreme events in the historical (1981-2000) and future (2081-2100) periods. SAM qualitatively reproduced CanESM2’s projected changes in EPI. To gain further insight into physical mechanisms, we performed “isolation runs” in which some of the CRM’s large-scale forcings were changed to their future values, while keeping all other forcings fixed to historical values. In all cases, long-term changes in horizontal advection were the dominant driver of projected decreases in EPI.

Dedication

Dedicated to my late mother **Mama' Mthethwa-Mpanza** who never witnessed me graduate from high school. Wangifundisa ubuntu, isimilo nokuthi umuntu, ungumuntu ngabantu. Owangifundisa khona kungefaniswe nanoma iziphi iziqhu zemfundo kodwa kungukuphila uqobo.

Acknowledgements

This work was funded by Environment and Climate Change Canada (ECCC) Contract No. 3000697135 and a Discovery Grant from the Natural Sciences and Engineering Research Council (NSERC). I thank my supervisor Professor Neil Tandon for his patient guidance and mentorship. Thank you for the knowledge you have shared with me, thank you for support beyond the laboratory. I acknowledge Megan Kirchmeier-Young in her role as scientific authority for the ECCC contract. I thank the committee members Professor Yongsheng Chen, Professor Rashid Bashir and Professor Gary Klaassen for their time and valuable feedback. I thank Devanarayana Rao for technical assistance with MATLAB coding. I thank Ji Nie (Peking University) for guidance regarding the Column Quasi-Geostrophic (CQG) modelling framework and Marat Khairoutdinov (Stony Brook University) for assistance with compiling Systems for Atmospheric Modelling (SAM). I thank Guilong Li and Yanjun Jiao at ECCC for assistance with obtaining Canadian Earth Systems Model version 2 (CanESM2) output. I thank the South African Weather Service (SAWS) for granting me a study leave to persue this degree.

Table of Contents

List of Tables

List of Figures

1. Chapter 1: Introduction

1.1 Extreme Precipitation Events and Associated Impacts

Extreme precipitation events (EPEs) and the associated flooding often have devastating effects on communities and livelihoods. EPEs vary regionally and seasonally, such that there are multiple definitions of extreme precipitation corresponding with multiple time scales (WMO, 2018). The World Meteorological Organization (WMO) recognizes two mainstream definitions of extreme precipitation: (1) precipitation exceeds a certain fixed threshold that is associated with a certain amount of impact, (2) rarity of the event, return period based or percentile-based threshold. In this study the definition of EPE in terms of return period is adopted. It must be stressed out that extreme precipitation and heavy rainfall are not the same. Heavy precipitation event may not be an EPEs.

The impact of EPEs is seen in infrastructure, food security and health, with reverberating effects through entire economic systems (IPCC, 2013). Extreme precipitation led to the Alberta floods of 2013, which affected approximately 100,000 people in 29 local jurisdictions and incurred approximately $5-6 billion in damages, making it the second costliest disaster in Canadian history (Milrad et al., 2017). The Pakistan floods of 2010 caused over 1900 fatalities and damaged over a million homes. The World Bank estimated that this disaster cost $9.7 billion in damages (Ahmed et al., 2011; Kronstadt et al., 2011). The record-breaking Texas floods of May 2015 resulted from the highest 5-day precipitation accumulations over that region in 68 years (Nie et al., 2018). In 2019, heavy rainfall claimed 42 lives and displaced thousands of people in Durban, on the east coast of South Africa (South African Weather Service, 2019).

The cases highlighted above are just a few of many examples in different regions around the world, and there is a great need to provide reliable projections of how the intensity of such extreme events will change in the future. In a warmer climate, the available moisture in the atmosphere is expected to increase in accordance with the Clausius-Clapeyron relation, resulting in increased intensity of both mean precipitation and extreme precipitation intensity over most regions (Trenberth, 1999; Trenberth et al., 2015). But this general expectation does not hold everywhere.

1.2 Extreme Precipitation in GCMs

Observations of extreme precipitation show that, over recent decades, the intensity of such events is increasing more rapidly than regional mean precipitation in most regions (Bao et al., 2017; Pfahl et al., 2017).

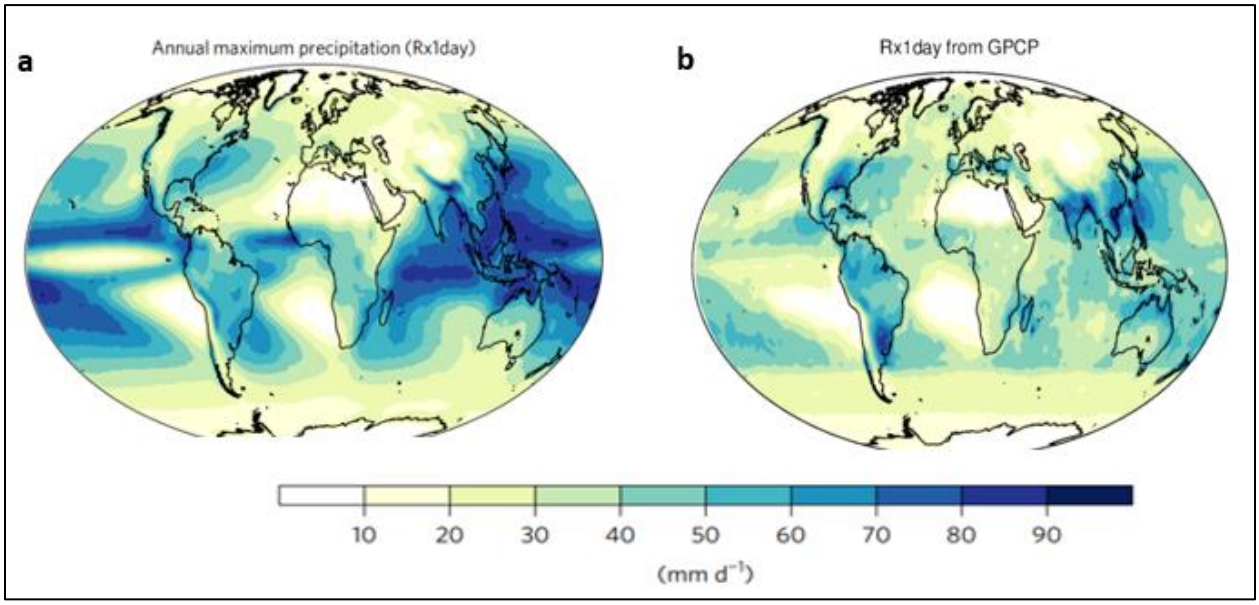

Figure 1: Present day extreme precipitation. (a) Annual maximum precipitation (Rx1day; from 22 CMIP5 model including CanESM2) in $\boldsymbol{mm \cdot d^{-1}}$, (b) Annual maximum precipitation (Rx1day; observations) from Global Precipitation Climatology Project (GPCP), both average over the period 1981-2000. Reproduced from Pfahl et al. (2017).

Pfahl et al, 2017 showed using 22 Coupled Model Intercomparison Project Phase 5 (CMIP5) (including CanESM2) models that simulated historical events in GCM (figure 1, panel a) compare very well in spatial patterns, but the strength is underestimated, panel b. Panel b is done using Global Precipitation Climatology Project (GPCP) dataset. This product is a blend of quality-controlled rain gauge, satellite, sounding data (Huffman et al., 1997). The underestimation of extreme precipitation in GCMs is expected since extreme events tends to occur in small scale convective clusters and such clusters are not well resolved in GCMs due to their parameterization and its mainly those convective clusters that results in extreme precipitation. GCMs are simulating spatial patterns reasonably well because they are associated with large scale systems which are well handled by GCMS.

Long-term increase in extreme precipitation intensity is observed even in regions where mean precipitation is showing a decreasing trend (Nie et al. 2018). Global climate models (GCMs) are also projecting an increase in extreme precipitation intensity over most of the globe (Pfahl et al., 2017). However, in some regions, long-term decreases in extreme precipitation intensity are projected. This regional variability is due to regional variations in projections of vertical velocity during extreme precipitation events (Pfahl et al., 2017; Tandon et al., 2018a), referred to as "extreme ascent."

Even though long-term increase in extreme precipitation is a well investigated topic, there is still a large gap on the seasonal patterns associated with these changes (Fischer and Knutti, 2016). Station data indicates a strong meridional variability, from 0%/K at 13ºS and 11ºN to above 10%/K at the equator and high latitudes (Westra et al., 2013). Rajczak et al. (2013) show that, over Europe there is a faster increase of extreme precipitation in winter compared to summer with South Europe showing a slight decrease of extreme precipitation during summer. Zheng et al. (2015) showed using rain gauge dataset between 1966 to 2012 over Australia that extreme daily precipitation has increase significantly during summer but decreased during fall.

Pfahl et al. (2017) show that the pattern and magnitude of the dynamical component is very different during summer than during winter. For this reason, climate change could also influence the seasonal cycle of extreme precipitation. Pfahl et al. (2017) indicates a possible global shift of the seasonality of extreme precipitation towards the cold season. Extreme daily precipitation could shift away from the middle of the summer towards the fall, but this is still unclear (Brönnimann et al., 2018; Marelle et al., 2018). Changes in seasonality of extreme precipitation have serious consequences on issues such as agricultural productivity, tourism industry, insurance companies, hydropower and water supply. Through complex interaction such as soil moisture dynamics and snow processes, changes in extreme precipitation can exacerbate flood risk (Marelle et al., 2018).

1.3 Dynamical Parameters Associated with Extreme Precipitation

Earlier studies have performed analysis suggesting that long-term changes in the horizontal scale of vertical velocity anomalies, referred to as "eddy length," are a key factor influencing regional extreme ascent projections (Tandon et al., 2018a; Tandon et al., 2018b). Eddy Length refers to

the horizontal length associated with ascending anomalies. Projected increases in eddy length are expected to weaken the coupling between convection and the large-scale vertical velocity, which in turn weakens extreme ascent, thereby reducing the precipitation intensity. These findings were based on analysis of output from state-of-the-art fully coupled GCMs. Eddy length can be associate with the static stability parameter linearly such that long-term changes (increase) in static stability also brings changes (increase) in the eddy length.

Understanding regional processes in GCMs is challenging due to the complexity of the models. Thermodynamic and dynamical coupling between adjacent atmospheric grid cells, as well as coupling between the atmosphere and the surface, makes it difficult to isolate mechanisms responsible for the projected extreme precipitation changes. Furthermore, GCMs have an inherent shortcoming in predicting individual events. They are intended to capture the long-term statistics of many extreme events (Randall et al., 2007; Pierce et al., 2009). This is due to the formulation, as well as the spatial and temporal resolutions used. Therefore, studying these events in GCMs only gives the statistical nature and the mean overview. Finer resolution regional models allow for controlled experimentation that can more easily isolate physical mechanisms relevant for extreme ascent, which are not captured in GCMs (Nie and Sobel, 2016).

1.4 Quasi-Geostrophic Omega Equation

The quasi-geostrophic omega (QGω) equation combines quasi-geostrophic vorticity, thermodynamic and continuity equations and it is diagnostic in nature. QGω permits a quantitative estimation of the vertical velocity field to be computed given the specification of the three-dimensional geostrophic flow field (Holton and Hakim 2012). One indication of its diagnostic value follows from noting that strong low-level ascent can promote cyclogenesis (at a synoptic scale), favouring the occurrence of precipitation (Davies, 2015). The QGω equation for wavelike disturbances can be written as:

$$\partial_{pp}\omega - \sigma\left(\frac{k}{f_0}\right)^2\omega = -\frac{1}{f_0}\partial_p Adv_\zeta + \frac{R}{p}\left(\frac{k}{f_0}\right)^2 Adv_T + \frac{R}{p}\left(\frac{k}{f_0}\right)^2 Q \quad (1)$$

Here, $adv(\cdot) = -u\partial_x(\cdot) - v\partial_y(\cdot)$ is the horizontal advection operator, where u and $v$are the horizontal winds in the x (zonal) and y (meridional) directions, respectively. Furthermore, $\zeta = \frac{1}{f_0}\nabla^2\phi + f$ is the geostrophic absolute vorticity, ϕ is the geopotential and f_0 is the reference value

of the Coriolis parameter. ∂_{pp} is the second partial derivative of pressure in the vertical, ω is the vertical velocity in pressure coordinates, σ- is the dry static stability, p is the pressur, ∇^2 is the horizontal Laplacian operator, Adv_ζ is the advection of large scale geostrophic absolute vorticity, R is the gas constant for dry air, Adv_T is the large scale horizontal advection of temperature, Q is the diabatic heating associated with convection and k is the inverse wavenumber associated by the length scale by $k = \frac{2\pi}{L}$. Equation 1 has been expressed in a wavenumber form which is slightly different from the traditional quasi-geostrophic omega equation expressed in a Laplacian form (Holton and Hakim 2012). The wavenumber form is related to the latter by recognizing that disturbances in the atmosphere maybe be viewed as wavelike. In this case the horizontal Laplacian is equivalent to k^2.

The Laplacian in the QGω plays a very important physical role, it acts to distribute the vertical velocity response to the forcing terms (Holton and Hakim 2012). This means that the vertical velocity response in each central grid will also carry information of the adjacent grids. This is of fundamental importance in the atmosphere since it is a continuum. One interpretation related to the role of the Laplacian is that ω responds to spatially averaged out gradients of the forcing terms rather than localized gradients. As a result, in synoptic scale motions uplift takes place in a column of air rather than small plumes.

QGω consists of three forcing terms on the right-hand side. The first term is the differential vorticity advection. When vorticity advection (VA) is increasing with height such that $\partial_p Adv_\zeta < 0$, then because of the negative sign in front of this term the result is $\omega < 0$ which is associated with upward. Downward motion (descent) will occur when VA is decreasing with height $\left(\partial_p Adv_\zeta > 0\right)$. Therefore, differential vorticity advection must be examined over the entire column (not just one level) to infer how it influences vertical velocity.

The second term on the RHs of (1) is the Laplacian of temperature advection (TA). During an episode of warm air advection (WAA), $Adv_T > 0$. Assuming a localized, wavelike anomaly, then $\nabla^2 Adv_T < 0$ and since there is a positive sign in front of this term, upward vertical velocity is forced $(\omega < 0)$. The opposite is true for cold air advection (CAA), $Adv_T < 0$. That is, the distribution of

TA is important when interpreting the forcing associated with this term. Upward motion associated with WAA is achieved through low level convergence and upper level divergence in accordance with the mass continuity equation $\left({}^{\partial u}/_{\partial x} + {}^{\partial v}/_{\partial y} = -{}^{\partial \omega}/_{\partial p}\right)$.

The first and second term on the rhs side when scaled tend to balance each other. This has a consequence of forcings associated with these terms either acting together or cancelling in certain regions of the atmosphere depending on the circulation (Funk, 2011). The last term on the rhs is diabatic heating term which is primarily convective heating on the time scales of interest. If the convective heating anomaly (Q) is positive, then $\nabla^2(Q) < 0$, so convective heating will force upward motion. On the lhs the key parameter is static stability (σ) which determines the vertical stability of the atmosphere. Small values of σ are associated with an unstable atmosphere while larger values are associated with stable conditions. σ parameter acts to determine whether for a given strength of forcing, will the atmosphere resist or support upward motion.

Multiplying equation 1 by a representative vertical pressure scale, ΔP^2 , and using the definition of the Rossby radius of deformation, $L_R = \frac{\sqrt{\sigma}\Delta P}{f_0}$ the second term on the lhs of (1) becomes $k^2 L_R^2$, which is the ratio of length scale and the Rossby radius of deformation. Under this scaling, terms two and three on the rhs are multiplied by a ratio $\frac{R\Delta P^2}{\sigma p}$. The physical interpretation is that when the length scale is less or comparable to the Rossby radius of deformation ($L \leq L_R$) there is coupling between large scale vertical velocity and convection. When the length scale is larger than the Rossby radius then the first term on the lhs balances with the first term on the rhs. Thus, vertical velocity is principally determined by differential vorticity advection and convection is decoupled from large scale. Based on equation (1), cyclonic differential vorticity advection (positive in the northern hemisphere) and positive temperature advection would positively force vertical velocity, resulting in ascent. Temperature advection is more important in the lower level of the atmosphere, while vorticity advection is prominent in the mid to upper levels. It is worth noting that cancellation between the first two terms on the rhs may be possible depending on the circulation. Over the subtropics where weather systems are both dynamical and convective in nature diabatic heating plays a significant role.

1.5 Convection Ingredients

There are three ingredients for convection to develop in the atmosphere: instability, moisture and a trigger to overcome stability in the boundary layer. All these three ingredients should overlap for a typical convection to develop, figure 2.

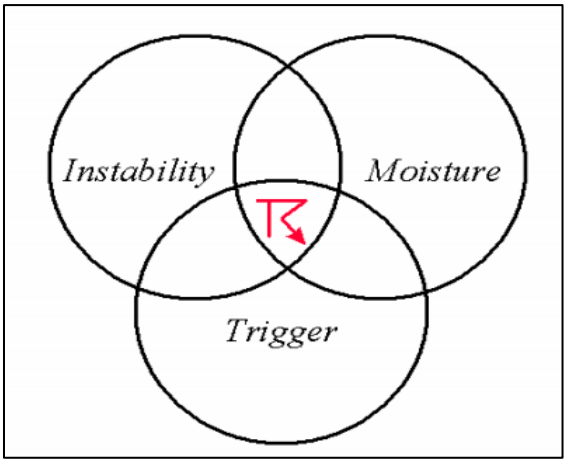

Figure 2: Schematic figure showing necessary (fundamental) ingredients for convection to take place in the atmosphere, source: Operational Techniques for forecasting thunderstorms.

Instability is needed for convection to take place. Instability is just the measure for the state of the atmosphere to permit or resist convection (American Meteorological Society, 2011). When the atmosphere is unstable any parcels of air lifted vertically will continue to rise and convection will take place provided there is enough moisture. Convective available Potential Energy (CAPE) is the standard measure of instability. There are other indices used to measure instability such as such as K-index, Showalter stability index, Total Totals index, etc. low level moisture is important because moist air is less dense than dry air and hence is more easily lifted when there is a trigger mechanism. Once lifted through adiabatic processes, condensation will take place above the lifting condensational level. The trigger mechanism may be orographic, frontal, dynamical or a feature such as a dryline.

1.6 Other Factor Influencing Extreme Precipitation

Several factors can influence the intensity of precipitation. Advective time scale of the large-scale flow given by $\tau = \frac{L}{U+U_0}$ is one example (Dwyer and O'Gorman, 2017). This parameter depends

on the zonal spatial extend (L) of the system as well as the strength of mean zonal velocity (U), meridional winds are accounted for indirectly by U_0. In an environment with weaker U , τ becomes large and that can be a factor on the intensity of precipitation especially at a temporal resolution of daily precipitation. Kidston et al. (2010) showed a robust increase of the length scale in a warmer climate. Such a robust increase will also result in an increase of advective time scale which can influence extreme precipitation intensity.

Tandon et al. (2018) showed that during an extreme precipitation event, the balance in QGω can be expressed as:

$$\partial_{pp}\omega_E - \frac{N_E^2\omega_E}{f^2L_E^2} = -\frac{1}{f}\partial_p Adv(\zeta_E) + \frac{R}{pf^2L_E^2}Adv(T_E') + \frac{RQ_E}{pf^2L_E^2}. \quad (2)$$

Where L is the eddy length and p is the pressure, N^2 represents static stability, Q is the diabatic heating, ω is the vertical velocity, ∂_p is the vertical partial derivative with respect to pressure, ∂_{pp} is the Laplacian in the vertical direction. The subscript E indicates on the day of extreme precipitation. Equation 2 is expressed in a format that outlines some of the key parameters that have an influence on extreme ascent and thus extreme precipitation. This equation still has the same meaning as equation 1. For wavelike disturbances, the horizontal Laplacian in the traditional form of the QGω equation becomes $\frac{1}{L^2}$.

When L is large, the diabatic and temperature advection terms and the stability term become small, as L appears on the denominator of equation 2. As $L \to \infty$, equation 2 reduces to $\partial_{pp}\omega_E = \frac{1}{f}\partial_p Adv(\zeta_E)$. This shows that for large L, extreme precipitation depends primarily on differential vorticity advection.

In this study, a dynamical downscaling approach is implemented using a cloud-resolving model (CRM; figure 4.) over a limited domain. Such an experimental design allows for finer control of the large scale forcings, such as the eddy length, stability and horizontal advections. We can perturb these forcings in such a way as to gain insight into the key processes responsible for changes in extreme precipitation intensity. Insights gained from such experiments can in turn motivate further improvements in GCM parameterizations, thereby improving confidence in model projections of extreme precipitation intensity. In this study, we focus on regions where dynamical

effects are expected to drive long-term decreases in extreme precipitation intensity. Improved understanding of such dynamical effects will lead to greater understanding of less dominant (but still important) dynamical effects in other regions.

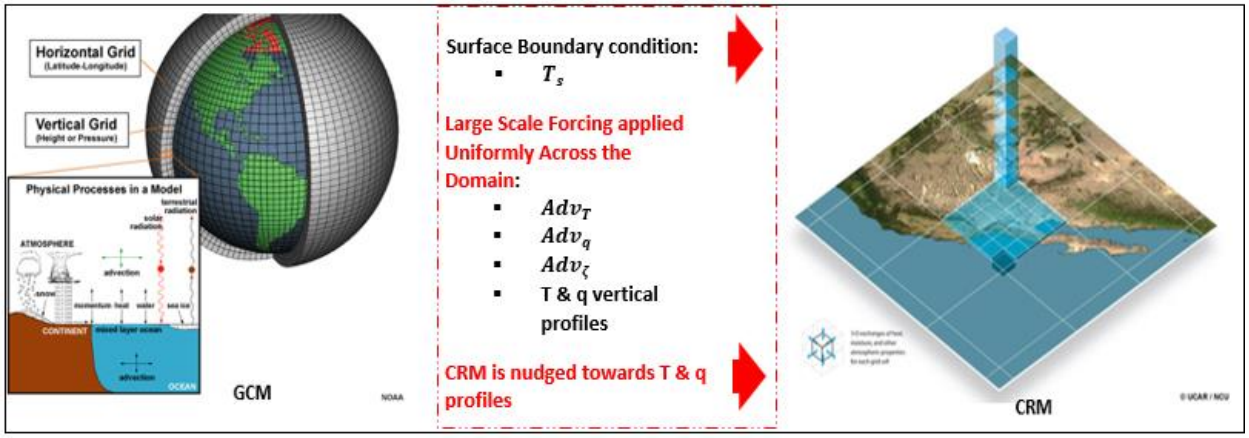

Figure 3: Schematic diagram showing the dynamical downscaling process and the variables necessary for the CQG framework. T is air temperature, q is moisture, T_s is sea surface temperature (surface temperature), $AdvT$ is temperature advection, $Advq$ is moisture advection and $Adv\zeta$ is advection of absolute vorticity. Adapted from images produced by NOAA and UCAR.

Our experiments suggest that, indeed, projected increase in eddy length does contribute to changes in extreme precipitation intensity. However, in particular regions, factors other than eddy length (especially horizontal advections) appear to play an even greater role in driving future decreases in extreme precipitation intensity. Results from such an experiment can not be used directly to make prediction, but we can potentially use results to improve understanding and performance of GCMs.

This document is organized as follows: Methods are explained in section 2, including descriptions of the modelling framework, forcing dataset and experimental design. In section 3, we present and discuss the results of our CRM experiments. Section 4 provides a summary of the key results and conclusions, along with ideas for future research.

2. Chapter 2: Methods

2.1 Model description

Our experiments utilize the column quasigeostrophic (CQG) framework, which relies on the (QGω) equation for wave-like disturbances (Nie and Sobel, 2016; Tandon et al., 2018a). In this formulation, coupling between convection and the large-scale vertical velocity is parameterized in terms of the eddy length, L, of the large-scale vertical velocity. Nie and Sobel (2016) performed model experiments showing that for smaller values of L (approaching the Rossby radius of deformation), coupling between convection and the large scale vertical velocity is especially strong. In this strongly coupled regime, as air rises, diabatic heating in the mid-troposphere acts to reduce the vertical stability at upper levels, resulting in deeper convection, stronger vertical motion, and longer, more intense precipitation events.

In this study, the CQG framework is implemented in a specific CRM called the System for Atmospheric Model (SAM; Khairoutdinov and Randall, 2003), with the details of the implementation described in Nie et al. (2018). SAM is a non-hydrostatic anelastic model, and we run it with a timestep of 10 s over a 128 km by 128 km domain with 2 km horizontal resolution and doubly periodic lateral boundaries. At such resolution, the CRM explicitly resolves convection within the domain. The model has 64 vertical levels with spacing ranging from 75 m near the surface to 500 m in the free troposphere.

At every time step, the horizontally averaged diabatic heating produced by the CRM is fed into the QGω equation along with imposed horizontal advection of temperature and absolute vorticity taken from a GCM. (The forcing data are described in more detail below). The QGω equation is then solved for the large-scale vertical velocity, which is used to compute large-scale temperature and moisture tendencies at every level, which are fed back into the CRM. In this way, the CRM captures coupling between convection and the large-scale vertical velocity, a key process that is missing in most previous dynamical downscaling studies. There is a discrepancy of the resolution between the driving GCM and the CRM, the GCM is a T63 model with a resolution of $2.8° \times 2.8°$ ($\approx 300km \times 300km$) while the CRM has a domain of $128km \times 128km$. This is taken care by applying large scale forcings evenly across the CRM domain. In this way the fact that the CRM domain is smaller than a single grid on the GCM is taken care off.

Figure 4 below shows a schematic diagram of the column quasi-geostrophic framework used in this experiment. One important parameter in this framework is the eddy length which can be tuned to strengthen or weaken the coupling between large scale and convection. L_R becomes the critical point that demarcates between coupled and decoupled regime, as explained under introduction.

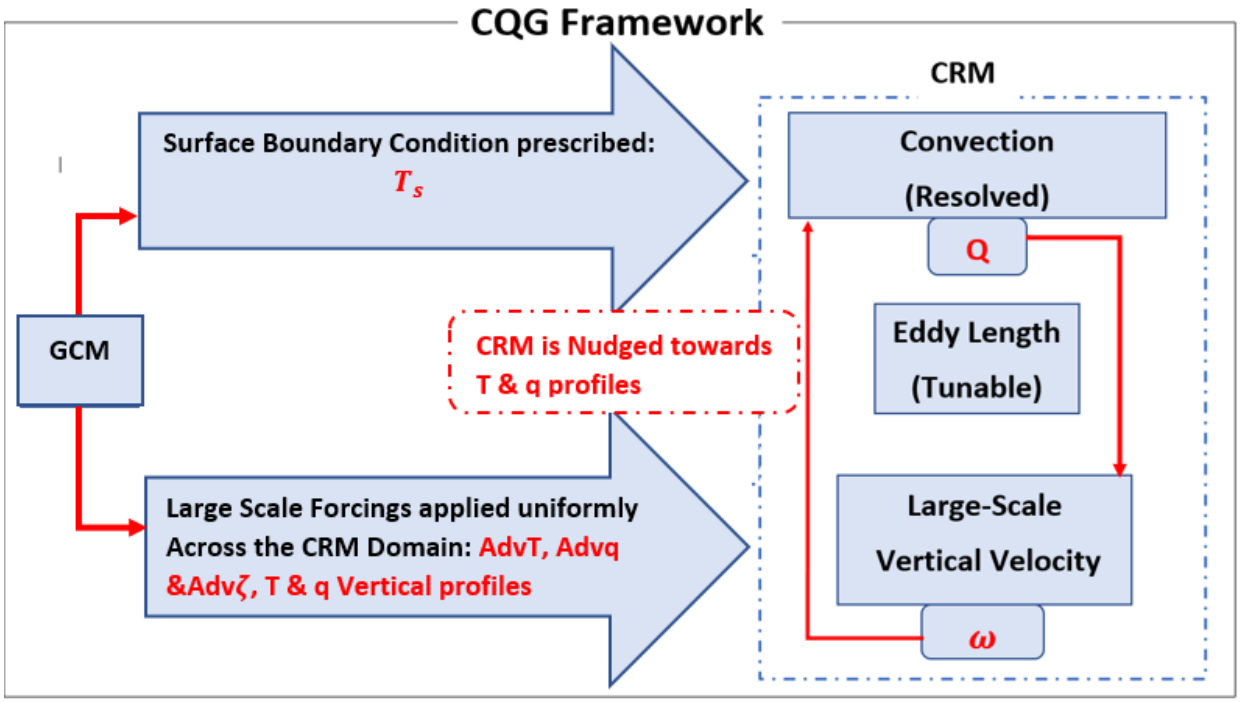

Figure 4: Schematic representation of the Column quasi-geostrophic framework, Q is the diabatic heating, Eddy length is the spatial scale of vertical velocity anomalies, ω is the large-scale vertical velocity calculated from the QGω equation. The T and q vertical profiles, T_s and the horizontal advection terms are derived from the Canadian Earth System model version 2 (CanESM2).

Insolation in the CRM varies with the diurnal cycle, but the daily mean insolation is held fixed to its daily mean value at the beginning of the simulation period. (We performed tests with seasonally varying insolation, and our results were not affected.) Surface temperature, T_s, is prescribed. Atmospheric radiative cooling in the CRM is mostly captured through the applied temperature profiles at the lateral boundaries. Radiation is fully interactive, updating at every model time step, 10 s. We use an ozone profile corresponding to the average ozone concentration over the month that the simulated event occurred. Ozone profiles are derived from the same emission scenario (Representative Concentration Pathways 8.5, RCP8.5) that was used to force CanESM2. RCP8.5

combines assumptions about high population and relatively low income growth with modest rate of technological and energy improvements leading to high greenhouse gas (GHG) emissions in the absence of climate change policy (Riahi et al., 2011).

2.2 Forcing data

SAM was forced with large scale temperature, moisture, geopotential and wind fields derived from output of the Canadian Earth System Model version 2 (CanESM2; Arora et al. 2011). CanESM2 is a fully coupled earth system model developed by the Canadian Centre for Climate Modelling and Analysis (CCCma). The atmospheric component of CanESM2 is a spectral model employing T63 triangular truncation, corresponding to approximately 2.8º X 2.8º horizontal resolution, with 35 vertical levels.

The model output used was from a 50-member ensemble of CanESM2 consisting of a historical (covering 1950-2005) and future (covering 2006-2100) simulation. Each member follows the high emission representative concentration pathway 8.5 (RCP8.5 scenario; Arora et al. 2011). Individual members differ by initial conditions. Therefore, an ensemble average will reduce the noise associated with the inherent internal climate variability. This has an advantage of producing a clearer response signal to externally forced climate change (Tandon et al., 2018a). Such model output is suitable for driving the current experiment since intermodel differences do not affect the analysis. Therefore, it becomes easy to perform experiments that can outline physical mechanisms using this model output. Using a different GCM other than CanESM can show different results due to differences in the formulation and parameterization schemes used (Pierce et al., 2009). This will also depend on the sensitivity of the model towards certain regions or processes.

In addition to using monthly mean surface air temperature (which we took to be equivalent to T_s), daily and 6-hourly output of air temperature (T), wind ($\mathbf{u}$), specific humidity (q) and geopotential (ϕ) were used. The 6-hourly data were archived on model sigma levels, and these were linearly interpolated to pressure levels required by the CRM.

Following Nie and Sobel (2016), we used 6-hourly CanESM2 output to compute the horizontal advective forcings required by the CRM. These advective forcings included the following:

1. Quasigeostrophic vorticity advection, $\mathrm{Adv}_\zeta = -\boldsymbol{U_g} \cdot \nabla \left[\frac{1}{f_0}\nabla^2\phi + f\right]$
2. Quasigeostrophic Temperature advection, $\mathrm{Adv}_T = -\boldsymbol{U_g} \cdot \nabla T$.
3. Quasigeostrophic Moisture advection, $\mathrm{Adv}_q = -\boldsymbol{U_g} \cdot \nabla q$.

Daily CanESM2 output was used to construct vertical profiles of potential temperature and moisture, which were additional large-scale forcings required by the CRM. All time-varying forcings were supplied to the CRM at the same temporal resolution as the CanESM2 output, and the CRM linearly interpolated these forcings in time. The surface boundary condition was prescribed as the seasonal mean of monthly surface air temperature (T_s), averaged over the 20-year epoch of interest (1981-2000 for the historical period and 2081-2100 for the future period). Here, the long-term seasonal average is taken including only month containing the extreme precipitation event of interest. We also tested running the CRM with daily varying SST corresponding to the precise dates surrounding the extreme precipitation events, and our results were not substantially different.

2.3 Eddy Length

Eddy length was computed from CanESM2 output following essentially the same procedure as in Tandon et al. (2018a):

1. On a given day of extreme precipitation at location (x, y), we computed the anomaly of daily mean vertical pressure velocity, ω, at 850 hPa with respect to the monthly climatology during the relevant epoch.
2. We then computed the zonal and meridional e-folding distances of this ω anomaly relative to (x, y), applying linear interpolation between grid point centres.
3. We divided the e-folding distances by $0.19 \times 2\pi$ to obtain the zonal and meridional scales of the corresponding waves, $L_x \; and \; L_y$ respectively, expressed as inverse wavenumbers. As shown by Barnes and Hartmann (2012), this factor arises from the fact that the e-folding distance of a cosine wave is 0.19 times its wavelength.

4. We combined $L_x \; and \; L_y$ to obtain an effective eddy length, $L_e = \left(\frac{1}{L_x^2} + \frac{1}{L_y^2}\right)^{-1/2}$.

The last step in this procedure is a refinement of the procedure used in Tandon et al. (2018a), who used $L_e = \sqrt{L_x^2 + L_y^2}$. While the latter is a heuristically reasonable approach, it is not mathematically consistent with how zonal and meridional wavenumbers are typically combined. The two approaches produce similar results.

Demonstrating this procedure by an example (i.e. at S27 location). We obtained $L_{e0} = 149$ km from CanESM2 during the historical period, and we obtained $L_e = 473$ km from CanESM2 during the future period. (We use the "0" subscript hereafter when referring to values during the historical period.) Accordingly, the fractional increase in eddy length squared between the historical and future periods, $\frac{\delta L_e^2}{L_{e0}^2} = \frac{L_e^2 - L_{eo}^2}{L_{e0}^2} = 907.7\%$. (We use δ hereafter when referring to changes between the historical and future periods.) This change normalized by the local change in surface temperature ($\delta T_s = 3.3$ K) yields 275.1% K^{-1}, which is much higher than the ensemble averaged projected changes in eddy length squared produced by CanESM2 in the subtropics in Tandon et al. (2018a).

An attempt to prescribe these eddy length values in the CRM was made, but in some cases such small horizontal eddy lengths created numerical instability in the CRM owing to unrealistically strong updrafts. Such numerical instability is not surprising, as CanESM2 parameterizes convection. Sensitivity of the convection scheme to large-scale forcing may be very different to the sensitivity of a convection-resolving model to the same large-scale forcing. In order for the CRM to run without numerical instability, we had to increase the eddy length by almost a factor of 4. This adjustment was applied to both the historical and future L_e values so that $\frac{\delta L_e^2}{L_{e0}^2}$ in the CRM runs matched $\frac{\delta L_e^2}{L_{e0}^2}$ in the GCM runs. Thus, in the CRM experiments presented below, we adjusted L_{e0} and $L_e$for the CRM runs to be numerically stable. Lower percentile extreme precipitation events were also investigated hoping to obtain longer spatial scales but there was no noticeable differences. Since some of the events investigated in this study have spatial scales that are close to the spatial resolution of CanESM2; their realism is questionable. Any unrealistic characteristics of the large scale forcings might generate numerical instability in the CRM.

2.4 Model experiments

Specific model experiments were constructed based on the results of Tandon et al. (2018a) and Tandon et al. (2018b), who examined regional variability of extreme precipitation projections in a large ensemble of CanESM2 simulations. Figure 5 below shows a composite climatic change of 10 year maximum of daily precipitation (Tandon et al., 2018b). Composite is an analysis (mostly statistical) of a large number of cases for a given climatological phenomenon. This is done to show the structure and characteristics of the phenomenon. Panel (a) shows a fractional change ($\frac{\delta P_e}{P_{eo}}$; of both the thermodynamic and dynamical part) normalized by zonal mean climatic change of annual surface temperature. P_E is the composite mean in 10-year maximum of daily precipitation, P_{E0} is $P_E$average over the historical period.

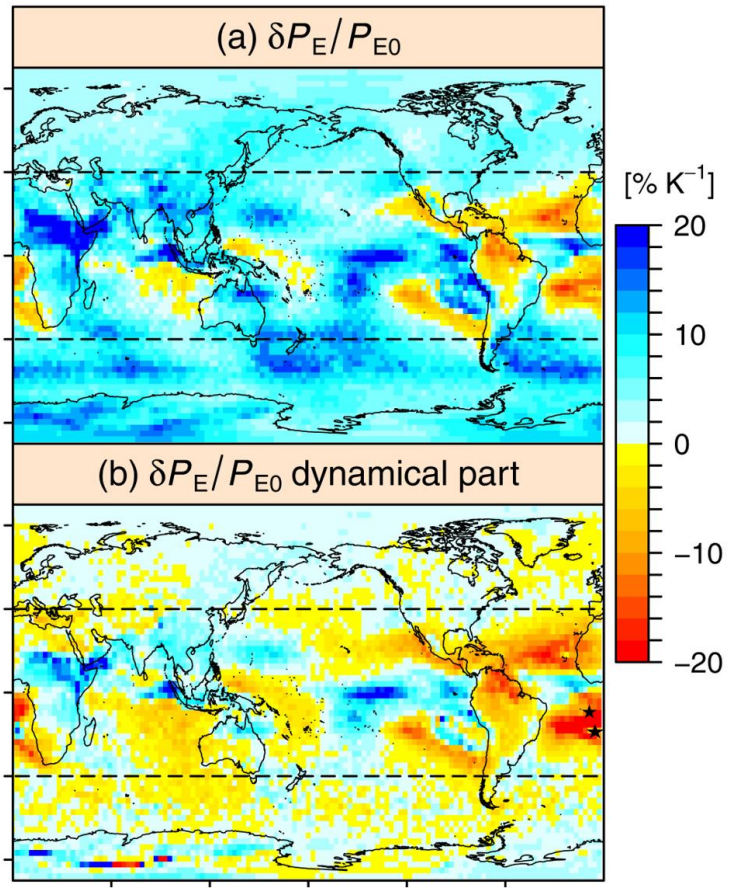

Figure 5: (a) Composite climatic change in 10 year maximum of daily precipitation in a large ensemble of CanESM2, adapted from Tandon et al., 2018. Panel (b) shows dynamical contribution to the extreme precipitation changes. See Tandon et al. (2018) for details of these calculations. These composites have been normalized by the zonal mean annual mean change in surface temperature. The stars indicate the locations used for the dynamical downscaling experiments in the current study (black corresponds to S27 and green to S18).

Physical scaling diagnostic is used to decompose regional changes in extreme precipitation into separate components (Pfahl et al., 2017). Extreme precipitation at a given location can be expressed by:

$$P_e \sim -\left\{\omega_e \frac{dq_s}{dp}\Big|_{\theta^* T_e}\right\} \quad (3)$$

Where P_e is extreme precipitation, ω_e the corresponding vertical velocity and $\{\cdot\}$ is a mass-weighted integral over the atmospheric column. This expression is evaluated at mean temperature during extreme precipitation. ω_e is the dynamic component of this expression (O'Gorman and Schneider, 2015). Tandon et al. (2018b) followed the same method but incorporated the factor r_E which slightly improves the agreement between the scaling and the model derived extreme precipitation in parts of the subtropics.

$$P_E = -\varepsilon\{\widehat{\omega_E} r_E S_E\} \quad (4)$$

$$P_{Eo} + \delta P_E = -\varepsilon\{(\widehat{\omega_{Eo}} + \delta\widehat{\omega_E})(r_{Eo} + \delta r_E)(S_{Eo} + \delta S_E)\} \quad (5)$$

Expanding the right-hand side and dividing by P_{eo} yields:

$$\frac{\delta P_E}{P_{Eo}} = \text{dynamical part} + \text{RH part} + \text{thermodynamic part} + \text{nonlinear part} \quad (6)$$

Where,

$$\text{dynamical part} = \frac{\{\delta\widehat{\omega_E} r_{Eo} S_{Eo}\}}{\{\widehat{\omega_{Eo}} r_{Eo} S_{Eo}\}} \quad (7)$$

$$\text{thermodynamic part} = \left\{\frac{\widehat{\omega_{Eo}} r_{Eo} \delta S_E}{\widehat{\omega_{Eo}} r_{Eo} S_E}\right\}. \quad (8)$$

The factor r_E is there to account for the fact that daily mean grid-scale relative humidity may be less than 100% on days of extreme precipitation. Most regions of the globe are showing an increase (light blue to deep blue) in extreme precipitation with exceptions over parts of the subtropics. Parts of the subtropics are showing a decrease in extreme precipitation (yellow to orange). Panel (b) shows only the dynamical part of the change. There is a strong signal of a decrease in extreme precipitation associated with the dynamical component, especially over the subtropics.

2.5 Case Selection

Following figure 3, two locations over the subtropical region were chosen for the experiment, first location: (26.5107ºS; 2.8125ºW, hereafter S27) and the second location (18.1389ºS;19.6875W, hereafter S18). These two locations are showing a strong projected weakening of extreme ascent and. Pfahl et al., 2017; Tandon et al., 2018a associate this with a projected decrease of extreme precipitation intensity. Twenty-year return period was used to select simulated extreme events in the GCM. The approach of using a return period is ideal for this study since the focus is on the cause of the change but not the probability of the event themselves. The return period chosen in this study was motivated by earlier studies (Tandon et al., 2018a) which grouped the study period for long term changes in epochs of 20-years. Should a 50 or 100-year return period be chosen this will have no effect on the results except that a much stronger signal might be associated with these higher return periods.

Table 1 contains a list of case names, dates of occurrence and eddy length used to run the CRM simulation. Case names are constructed such that the first three letters represent the location (S27; ~27º South), second two represent ensemble member realization (r5; the member comes from realization 5), the middle four represent epoch (Hist; Historical, 1981-2000) and the last three represent the parent model (GCM; Global Climate Model), therefore the resulting case name is S27r5-Hist-GCM.

Table 1: Descriptions of the GCM simulations examined in this study.

Case Name	Date of Extreme Precipitation Event	Eddy Length (km)	Location
S27r1-Hist-GCM	24 September 1997	796	26.51ºS; 02.83ºW
S27r1-Fut-GCM	30 September 2094	2534	26.51ºS; 02.83ºW
S27r2-Hist-GCM	1 July 1982	637	26.51ºS; 02.83ºW
S27r2-Fut-GCM	2 April 2093	988	26.51ºS; 02.83ºW
S18r2-Hist-GCM	10 May 1981	1114	18.14ºS; 08.44ºW
S18r2-Fut-GCM	19 June 2092	1023	18.14ºS; 08.44ºW
S18r4-Hist-GCM	13 May 1982	1114	18.14ºS; 08.44ºW
S18r4-Fut-GCM	16 June 2084	703	18.14ºS; 08.44ºW
S27r5-Hist-GCM	29 June 1982	557	26.51ºS; 02.83ºW
S27r5-Fut-GCM	12 April 2082	498	26.51ºS; 02.83ºW
S18r5-Hist-GCM	31 March 1987	716	18.14ºS; 08.44ºW
S18r5-Fut-GCM	28 September 2087	486	18.14ºS; 08.44ºW

The eddy length values computed from the GCM are mostly small compared to the Rossby radius (L_R). L_R is defined as the scale at which rotational effects in the atmosphere become as important as buoyancy or gravity wave effect (American Meteorological Society 2011). L_R has a characteristic scale of 10^6 and most of the eddy length scales calculated here are of the order 10^5. When the eddy length is less than L_R the disturbances are mesoscale. This is good for this experiment since the CRM is used to explicitly resolve convection. The fact that some of the eddy length values calculated from the GCM are comparable to the GCM horizontal resolution makes the confidence in the physics governing these extreme events questionable.

Figure 6 shows a timeseries of annual maximum of daily precipitation from CanESM2 over the SSA region during the historical (black) and future (red) periods. These timeseries correspond to the cases named S27r1-Hist-GCM and S27r1-Hist-GCM. Comparison of the two timeseries shows that the 20-year maximum of daily precipitation (P_e, within the green triangles) is reduced by about 33% in the future period compared to the historical period. Such a strong decrease is in

stark contrast with the increase in extreme precipitation intensity over most other regions, and thus these S27r1 cases are suitable choices for further investigation of the dynamical mechanisms influencing extreme precipitation projections. The simulated historical extreme precipitation event is dated September 27,1997 and the future extreme precipitation event is dated September 30, 2084.

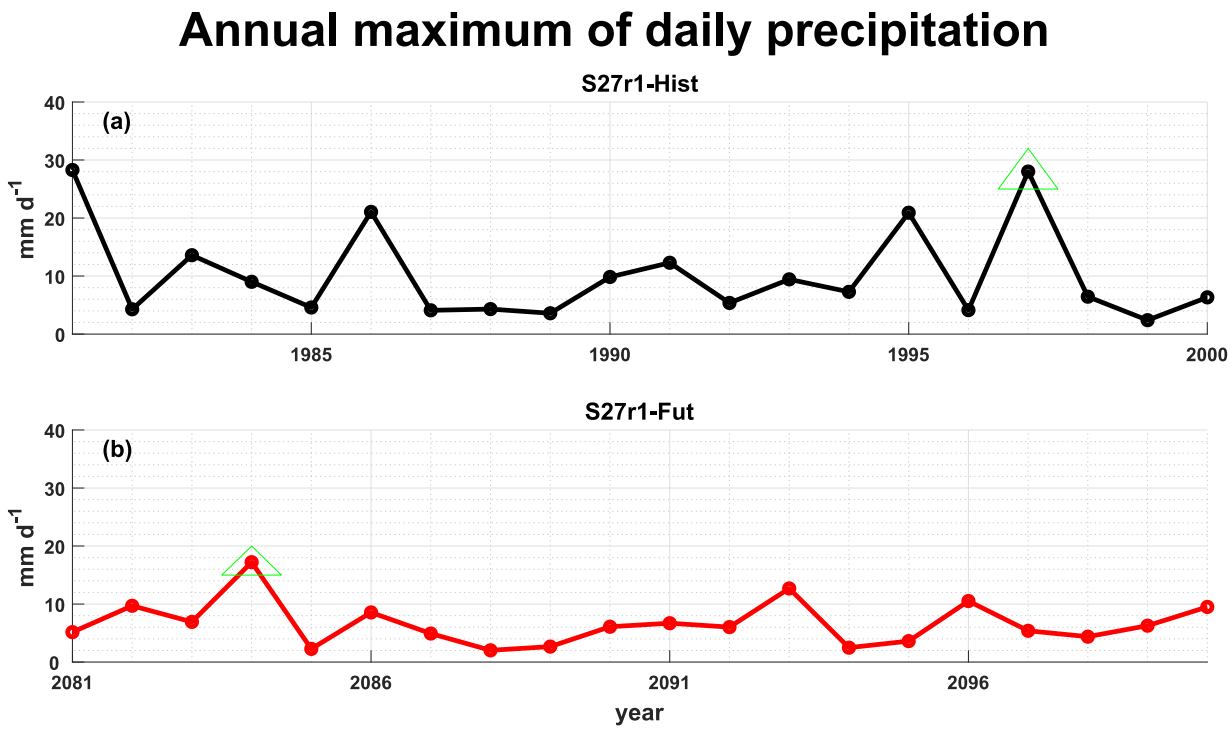

Figure 6: Timeseries of annual maximum daily precipitation over the S27 region (26.510°S, 2.8125°W) in CanESM2 during the (a) historical period (1981-2000) and (b) future period (2081-2100). The green triangles indicate the 20-year maximum events chosen for the CRM experiments. See the text for additional details.

Using the CanESM2 forcing fields derived as described in previous sections, we ran the CRM for both the historical and future cases. The following cases were run S27r1-Hist, S27r1-Fut, S27r2-Hist, S27r2-Fut, S27r5-Hist, S27r5-Fut, S18r2-Hist, S18r2-Fut, S18r4-Hist, S18r4-Fut, S18r5-Hist and S18r5-Fut. In each case, we ran the model for 10 days with only the temperature and moisture profiles applied, which allows the CRM to reach a state of radiative-convective equilibrium. Thereafter, the additional CQG forcings (Adv_ζ, Adv_q, Adv_T) are turned on, beginning 15 days before the extreme precipitation event and continuing for 15 days after the extreme precipitation event.

3. Chapter 3: Results and Discussions

3.1 Tabular Form of Results

Table 2 contains numerical values of all the CRM experiments as well as the naming used for different simulations.

Table 2**:** Numerical results of the CRM experiments. Changes between the historical and future periods are indicated by δ. Time adjustment is the number of days that the CRM precipitation time series was shifted to facilitate comparison of extreme precipitation intensity. E.g., "+1d" means the CRM was simulating extreme precipitation 1 day early compared to the GCM.

Historical Case	Future case	Timing Adjustment		P_{e0} (Historical)	P_e(Future)	$\delta P_e/P_{e0}$	δT_s	$\delta P_e/P_{e0}/\delta T_s$
		Hist	Fut	[mm d^{-1}]	[mm d^{-1}]	[%]	[K]	[% K^{-1}]
S27r1-Hist-GCM	S27r1-Fut-GCM			28.02	17.22	−38.5	3.3	−11.7
S27r1-Hist	S27r1-Fut	+1d	none	61.54	45.06	−26.8	3.3	−8.1
S27r1-Hist	S27r1-ΔL	+1d	none	61.54	72.35	17.6	3.3	5.3
S27r1-Hist	S27r1-Δ$Stab.$	+1d	none	61.54	67.13	9.1	3.3	2.8
S27r1-Hist	S27r1-ΔAdv	none	none	61.54	22.86	-62.9	3.3	-19.1
S27r2-Hist-GCM	S27r2-Hist-GCM			23.64	12.55	-46.9	4.9	-9.6
S27r2-Hist	S27r2-Fut-	+1d	+1d	71.26	52.11	-26.9	4.9	-5.5
S27r2-Hist	S27r2-ΔL	+1d	none	71.26	81.09	+13.8	4.9	+2.8
S27r2-Hist	S27r2-Δ$Stab.$	+1d	none	71.26	75.78	+6.3	4.9	+1.3
S27r2-Hist	S27r2-ΔAdv	+1d	none	71.26	30.72	-56.9	4.9	-11.6
S18r2-Hist-GCM	S18r2-Hist-GCM			38.9	3.7	-90.5	1.8	-50.2
S18r2-Hist	S18r2-Fut	+1d	+2d	28.53	40.24	+41.0	1.8	+22.8
S18r2-Hist	S18r2-ΔL	none	none	28.53	28.16	-1.3	1.8	-0.5
S18r2-Hist	S18r2-Δ$Stab.$	none	none	28.53	26.39	-7.5	1.8	-4.2
S18r2-Hist	S18r2-ΔAdv	+2d	none	28.53	42.12	47.6	1.8	+26.4
S18r4-Hist-GCM	S18r4-Fut-GCM			8.67	5.07	−41.6	0.9	-46.2
S18r4-Hist	S18r4-Fut	none	+2d	48.41	11.44	−76.4	0.9	-84.9
S18r4-Hist	S18r4-ΔL	none	none	48.41	38.98	-19.5	0.9	-21.7
S18r4-Hist	S18r4-Δ$Stab.$	none	none	48.41	46.22	4.5	0.9	+5.0
S18r4-Hist	S18r4-ΔAdv	+2d	none	48.41	8.43	-82.6	0.9	-91.8
S27r5-Hist-GCM	S27r5-Fut-GCM			30.52	10.06	-67.0	4.7	-14.3
S27r5-Hist	S27r5-Fut	+1d	none	30.75	12.59	-59.1	4.7	-12.6
S27r5-Hist	S27r5-ΔL	none	none	30.75	27.18	-11.6	4.7	-2.5
S27r5-Hist	S27r5-Δ$Stab.$	none	none	30.75	27.33	-11.1	4.7	-2.4
S27r5-Hist	S27r5-ΔAdv	+1d	none	30.75	27.74	-9.8	4.7	-2.1
S18 r5-Hist-GCM	S18r5-Fut-GCM			10.49	2.82	-73.1	-1.4	52.2
S18 r5-Hist	S18r5-Fut	none	+2d	39.57	41.84	+5.7	-1.4	4.1
S18 r5-Hist	S18r5-ΔL	none	none	39.57	25.51	-35.5	-1.4	25.4
S18 r5-Hist	S18r5-Δ$Stab.$	none	none	39.57	30.70	22.4	-1.4	16.0
S18 r5-Hist	S18r5-ΔAdv	+2d	none	39.57	54.13	+36.8	-1.4	26.3

Throughout the discussion this table will be used together with the figures for better comparison. The table represents a complete set of simulations that were run, not all figures are presented in this document, but the table contain all the simulations. Column 1-2 is the naming of the cases. Column 3 is time adjustment which shows by how many days was the precipitation timeseries was time shifted so that the day of maximum precipitation aligns with that in the GCM runs to facilitate comparison. Column 4-5 are the precipitation amounts for historical and future respectively. Column 6 is the precipitation change in percentages. Column 7 (δT_s) is the change is surface temperature between the two epochs (1981-2000;2081-2100). In some cases, the pair of events occurred in different seasons, this makes δT_s values to be either very small, below one or very large (e.i. $\sim 5K$. The last column is the fractional change in extreme precipitation normalized by surface temperature.

3.2 Model Evaluation

Having identified the cases of interest from the GCM, simulations were performed to assess how well the CRM reproduced these cases, figure 7. Six experiments were simulated over two locations S27 and S18 over the subtropics. Each pair of simulations is driven by different ensemble member for large scale forcings. Figure 7a shows the comparison between the historical case S27-Hist (red) and the GCM (S27-Hist-GCM; blue). The CRM precipitation here and in all analysis below corresponds to the precipitation horizontally averaged over the CRM domain. Ensemble mean was taken to account for the uncertainty associated with the CRM simulations. All results that will be presented here will be in a form of an ensemble mean with few exceptions in cases where individual members showed a unique and interesting feature that are not captured by the ensemble plots.

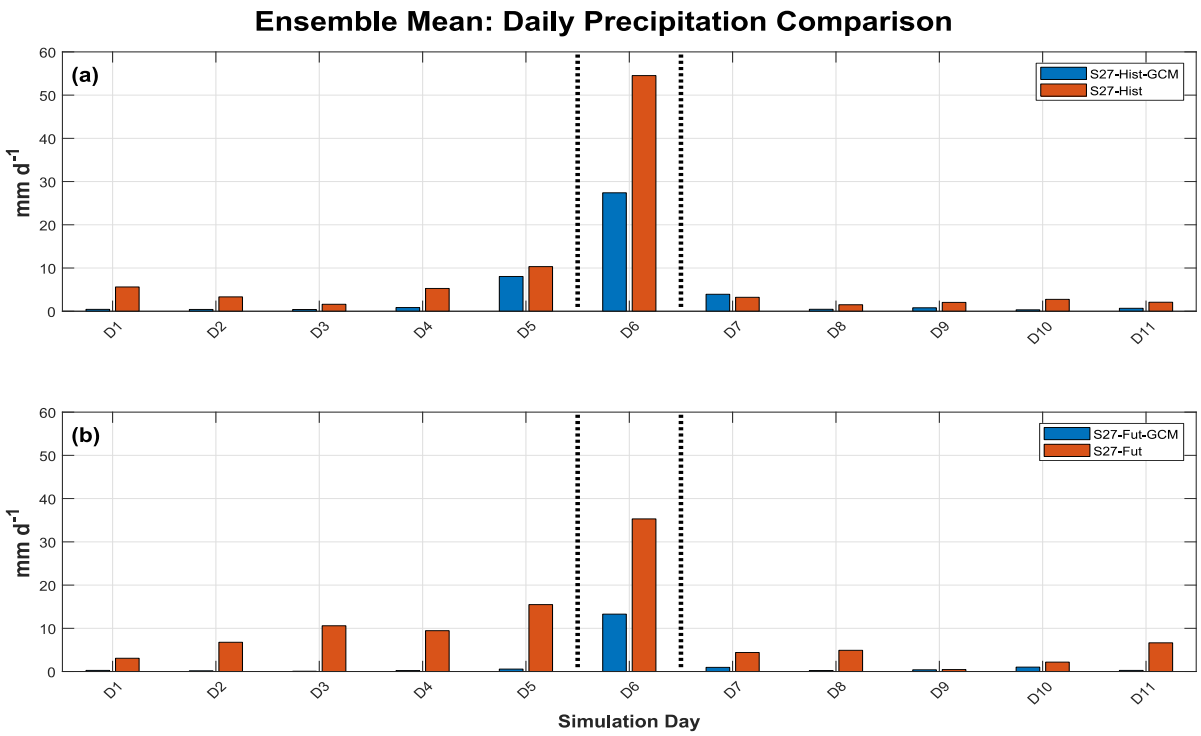

Figure 7: Ensemble mean comparison of the GCM and CRM daily precipitation timeseries for the 11-day periods centered around the 20-year maxima of extreme precipitation (day 6, between the vertical dotted lines) in CanESM2 over the S27 region. (a) S27-Hist-GCM (blue) and S27-Hist (red) cases. (b) The S27-Fut-GCM (blue) and S27-Fut (red) cases. To facilitate the comparison of extreme precipitation intensities some CRM timeseries have been time shifted by 1-2 days so that the day of maximum precipitation aligns with that in the GCM runs. These details are provided in Table 2 and the text.

Quantitatively, the CRM is overestimating the GCM precipitation in both the historical and future simulations. The peak precipitation of S27-Hist comes one day earlier than in S27-Hist-GCM while the S27-Fut-GCM and S27-Fut the CRM captured the timing, figure 7. Such a difference in timing is not surprising, as the GCM parameterizes convection, whereas the CRM explicitly resolved convection. Khairoutdinov and Randall (2003) also noted the same timing issue when they were evaluating the model SAM. Similar behaviour is shown by the CRM at the location 18S, figure 8 below. However, the CRM is able to capture the decrease in projected extreme precipitation intensity from historical to future in both locations.

One simulation showed simulations (individual member: S27r5-Hist, S27r5-Fut; see table 2) where the CRM did very well in capturing the intensity of the events. What distinguish this simulation from the rest is that the eddy length is decreasing from historical to the future (as

calculated from the GCM), see eddy length scale values in table 1. Two other unique cases; in these cases, the CRM reproduced an increase in extreme precipitation opposite to the GCM (figure not shown; S18r2 and S18r5), see table 2 for a complete set of cases. Generally, the CRM overestimated precipitation intensity but capturing the decrease in the projected intensity when an ensemble mean is taken. The ability of the CRM to capture this trend is a good motivation to proceed with the experiment and investigate the physical mechanisms responsible. Cases where the CRM captured an increase rather than a decrease in extreme precipitation are also interesting to investigate further to establish the responsible mechanisms for a cross comparison at the end.

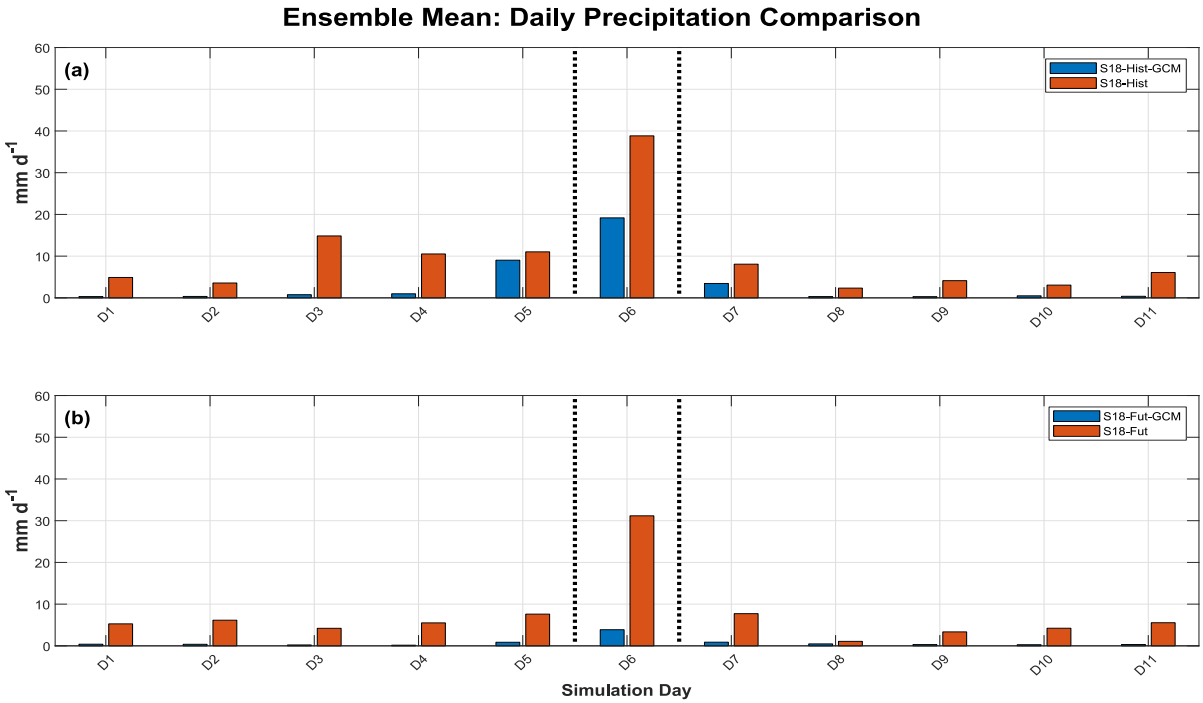

Figure 8: Ensemble mean comparison of the GCM and CRM daily precipitation timeseries for the 11-day periods centered around the 20-year maxima of extreme precipitation (day 6, between the vertical dotted lines) in CanESM2 over the S18 region. (a) S18-Hist-GCM (blue) and S27-Hist (red) cases. (b) The S27-Fut-GCM (blue) and S27-Fut (red) cases. To facilitate the comparison of extreme precipitation intensities some CRM timeseries have been time shifted by 1-2 days so that the day of maximum precipitation aligns with that in the GCM runs. These details are provided in Table 2 and the text.

3.3 Isolation Runs

To investigating the mechanism responsible for the changes in extreme precipitation we performed isolation runs. Isolation run is defined as running the model with the exact configuration but only changing one parameter, then the resulting change in the simulated time series is

associated with the parameter that was changed. Eddy length, stability and advection are the three parameters that were changed independently. These three parameters are associated with projected decrease in extreme precipitation intensity (Loriaux et al., 2017; Tandon et al., 2018b). Refer to table 2 for the naming and numerical values of the isolation runs. Figure 9 below shows the comparison of the isolation runs. Each panel answers a single question out of the three main questions that the experiment is attempting to address.

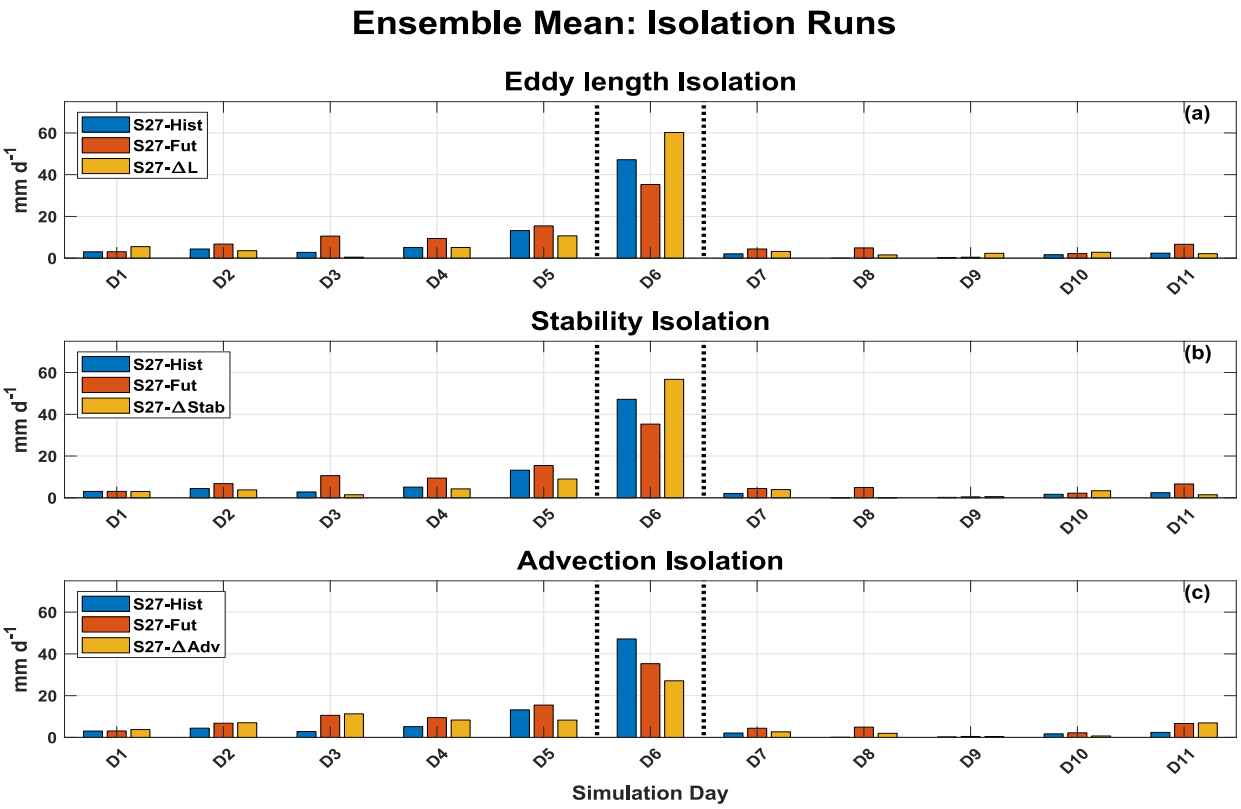

Figure 9: Ensemble mean comparison of daily precipitation timeseries for various CRM experiments. (a) The S27-Hist (blue), S27-Fut (red) and S27-ΔL, isolating the eddy length effect (yellow). (b) The S27-Hist (blue), S27-Fut (red) and S27-Δ$Stab$, isolating the stability effect (yellow). (c) The S27-Hist, S27-Fut and S27-ΔAdv, isolating advection effects (yellow). The day of the extreme precipitation in the GCM (day 6) lie between the vertical dotted lines. To facilitate the comparison of extreme precipitation intensities some CRM timeseries have been time shifted by 1-2 days so that the day of maximum precipitation aligns with that in the GCM runs. These details are provided in Table 2 and the text.

The first question was, ‘’what happens to the projected extreme precipitation intensity when all parameters are kept the same and only apply the change in eddy length’’. See section 3.3 under methodology for the calculation of the eddy length change. Figure 9a shows the comparison of the eddy length isolation simulation with the historical and future simulations. The change in eddy length appeared to cause an increase in extreme precipitation intensity (yellow). Studying the

QGω equation (equation 2), we see that extreme ascent is a dynamical parameter influenced by horizontal advections and diabatic heating (Nie and Sobel 2016a). Changes in extreme ascent are associated with the changes in extreme precipitation when evaluating the dynamical component (Tandon et al., 2018b). This expression shows that for a weather system with a large eddy length the balance in equation 2 will be mainly between the terms on the lhs side and the first term in the rhs (vorticity advection). Therefore, the increase that is seen in figure 9a may be an indication that this system is an advection driven system. Large eddy length may also increase extreme precipitation in terms of advective time scale (τ, Dwyer and O'Gorman, 2017).

Larger length scale results in a larger τ which means the system will be affecting one location for prolonged duration and that may contribute to extreme precipitation.

However, there were cases where changes in eddy length are resulting in a decrease in extreme precipitation, figure 10a. This becomes apparent when the system is convectively driven. An increase in eddy length to values larger the Rossby radius of deformation (L_R) weakens the coupling between large scale and convection (Nie and Sobel 2016). When the system becomes decoupled there is no positive feedback such that the system decays faster and extreme ascent weakens. Combining these results, a preliminary conclusion is that an increase in eddy length is not the principal driver associated with a decrease in projected extreme precipitation. However, it's worth noting that in some locations within the subtropics, eddy length does show a weaker decrease in extreme precipitation intensity. The effect of eddy length change may be dependent on the nature of the system that is being investigated as well as the geographical region. Further meteorological analysis is needed to evaluate whether the system in question is predominantly convective or large scale driven.

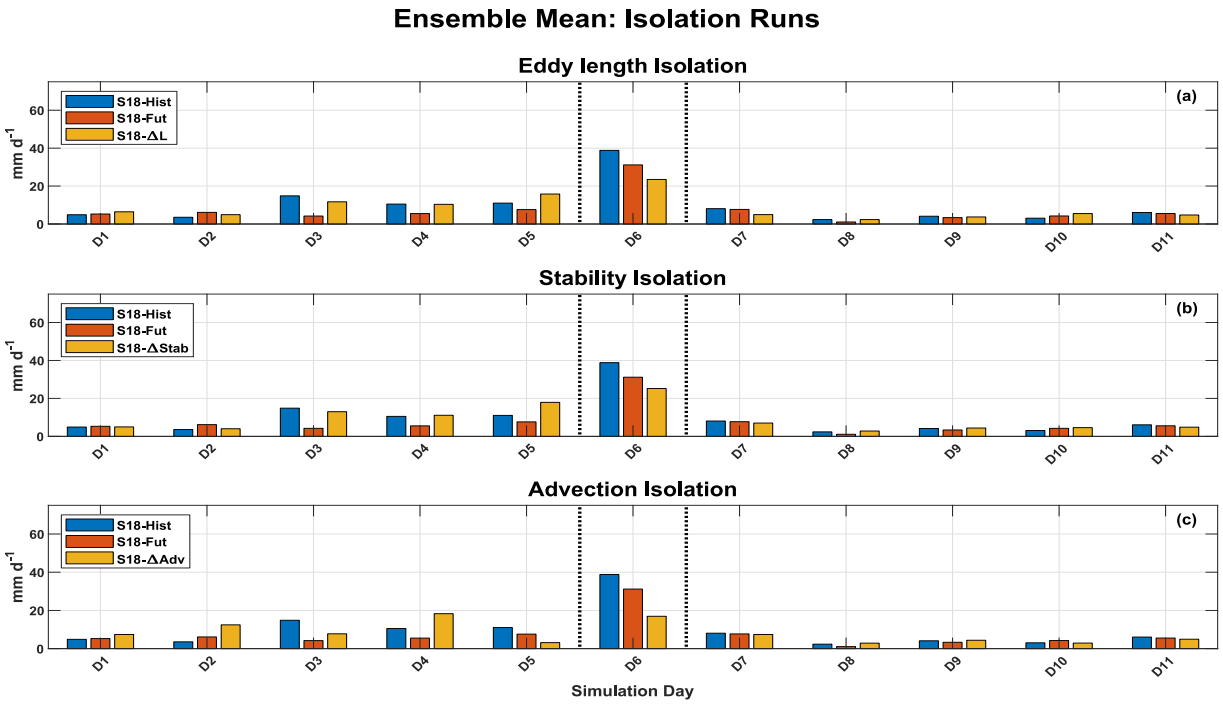

Figure 10: Comparison of daily precipitation timeseries for various CRM experiments. (a) The S18-Hist (blue), S18-Fut (red) and S18-ΔL, isolating the eddy length effect (yellow). (b) The S18-Hist (blue), S18-Fut (red) and S18-$\Delta Stab$, isolating the stability effect (yellow). (c) The S18-Hist, S18-Fut and S18-ΔAdv, isolating advection effects (yellow). The day of the extreme precipitation in the GCM (day 6) lie between the vertical dotted lines. To facilitate the comparison of extreme precipitation intensities some CRM timeseries have been time shifted by 1-2 days so that the day of maximum precipitation aligns with that in the GCM runs. These details are provided in Table 2 and the text.

The second question was, ‘’what happens to projected extreme precipitation intensity when all variables are kept the same but only applying changes in atmospheric stability. Figure 9b and 10b show the comparison between stability isolation, historical and future simulations. Changes in stability showed a weak increase in extreme precipitation (figure 9b) while in figure 10b it shows a weaker decrease. Dynamically an increase in stability is associated with weakening between convection and large-scale vertical velocity, this in turn is expected to decrease extreme precipitation intensity due to the lack of positive forcing to vertical velocity from convective heating. A preliminary conclusion here was that stability alone does not play a principal role in the projected decrease in extreme precipitation over the subtropics and its small influence can change from location to location.

The third question was, ‘’what happens to projected extreme precipitation intensity when all variables are kept the same only applying a change in advection’’. Figure 9c and 10c are the

comparison between horizontal advection isolation, historical and future simulations. In both locations horizontal advection isolation showed a quantitively big decrease in extreme precipitation intensity. This decrease is comparable to the decrease shown by the GCM and sometimes its stronger. All the individual members at location S27 showed a decrease in extreme precipitation when the change in vorticity advection was applied, but not all cases at S18 showed this. This might be an indication that the nature of weather systems associated with these extreme precipitating events are different in these two locations.

Cyclonic vorticity advection affects a weather by inducing some rotation which promotes low-level convergence and upper level divergence; when this takes place vertical velocity within a column is induced. The QGω tells us that advection may have both an amplifying and breaking effect on extreme precipitation depending on the circulation and the vertical distribution of differential absolute vorticity advection. Both differential absolute vorticity and temperature advection are vital over the subtropics where dry dynamics dominate (Nie and Sobel, 2016).

Another important factor is that changes in advection may be associated directly with changes in circulation. When the circulation is strong and highly baroclinic it is expected that the advective terms of the QGω will be dominant. In a weaker circulation these terms will be contributing less to vertical velocity. In this case it's possible that the zonal winds are weakening over the westerly regime in the future and undergoing a poleward shift. The preliminary conclusion is that advection is playing a principal role in the projected decrease of extreme precipitation intensity and it's not straightforward what can be influencing this but based on the literature, this change may be broadly associated with the changes in the large scale circulation such as the weakening of zonal winds influencing changes in the advective forcing terms of the QGω equation. Also, their appear to be a dependency on the nature of the weather system. It will be worth in the future to perform these isolation experiments independently in large scale driven and convective events and compare the differences side by side.

3.4 Advection Isolation

Trying to refine and narrow down the responsible mechanisms additional isolation runs focusing on the advective terms only were conducted. These isolation runs focused on individual terms

advective terms (temperature, moisture and total vorticity). This was done to quantify the contribution of each term in the QGω. Moisture advection was also included in these isolation experiment even though it does not appear on the QGω equation. Moisture advection can influence extreme precipitation by increasing the moisture content of the column. This typically becomes a secondary factor amplifying an already existing event. The parameterization of large scale in this experiment is implemented in a manner that permits the input of moisture advection into the CRM system via the moisture tendency equation.

Defining this set of isolations; all parameters were kept the same only applying the change in one advective term at a time. These set of runs are different from the initial advection isolation runs because they look at the effect of individual forcing terms. This analysis becomes relevant when following Trenberth's reasoning which outlines a possibility of strong cancellation between differential absolute vorticity and temperature advection term. Figure 11a-c and 12a-c show isolation runs corresponding to advection of temperature, moisture and differential absolute vorticity, respectively.

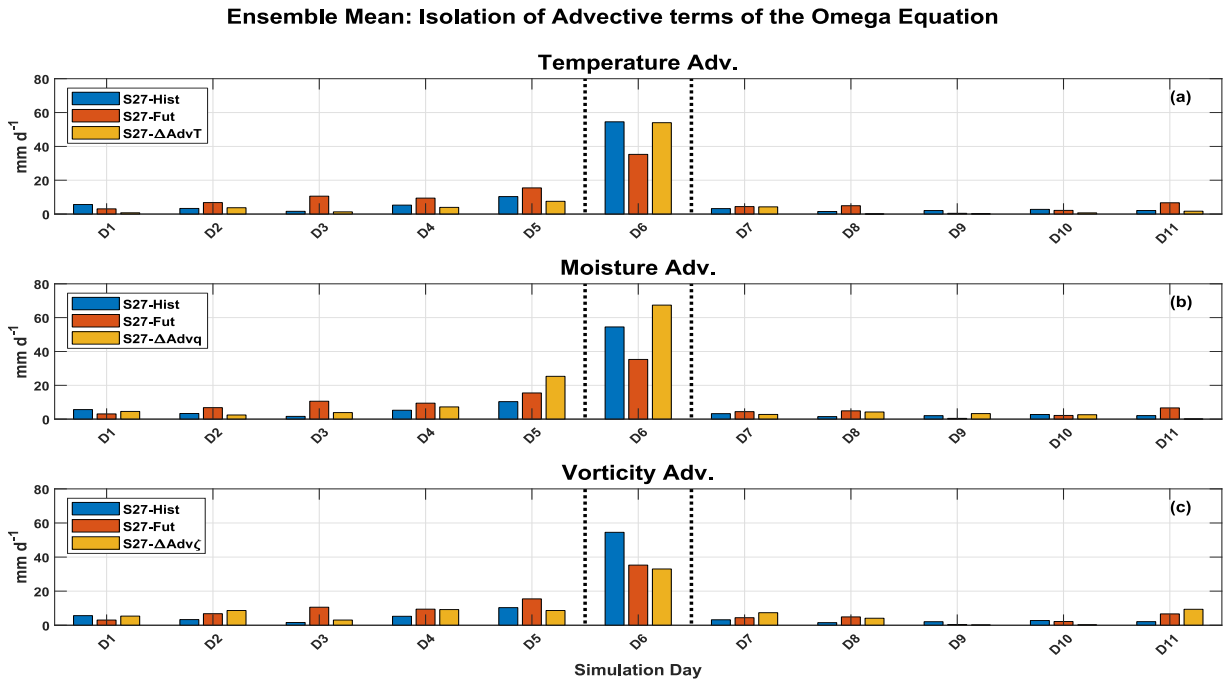

Figure 11: Comparison of daily precipitation timeseries for various CRM experiments. (a) The S27-Hist (blue), S27-Fut (red) and S27-$\Delta TAdv$, isolating the eddy length effect (yellow). (b) The S27r1-Hist (blue), S27-Fut (red) and S27-$\Delta qAdv$, isolating the stability effect (yellow). (c) The S27-Hist, S27-Fut and S27-$\Delta VortAdv$, isolating advection effects (yellow). The days of the extreme precipitation in the GCM (day 6) lie between the vertical dotted lines. To facilitate the comparison of extreme precipitation intensities some CRM timeseries have been time shifted by 1-2 days so that the day of maximum precipitation aligns with that in the GCM runs. These details are provided in Table 2 and the text.

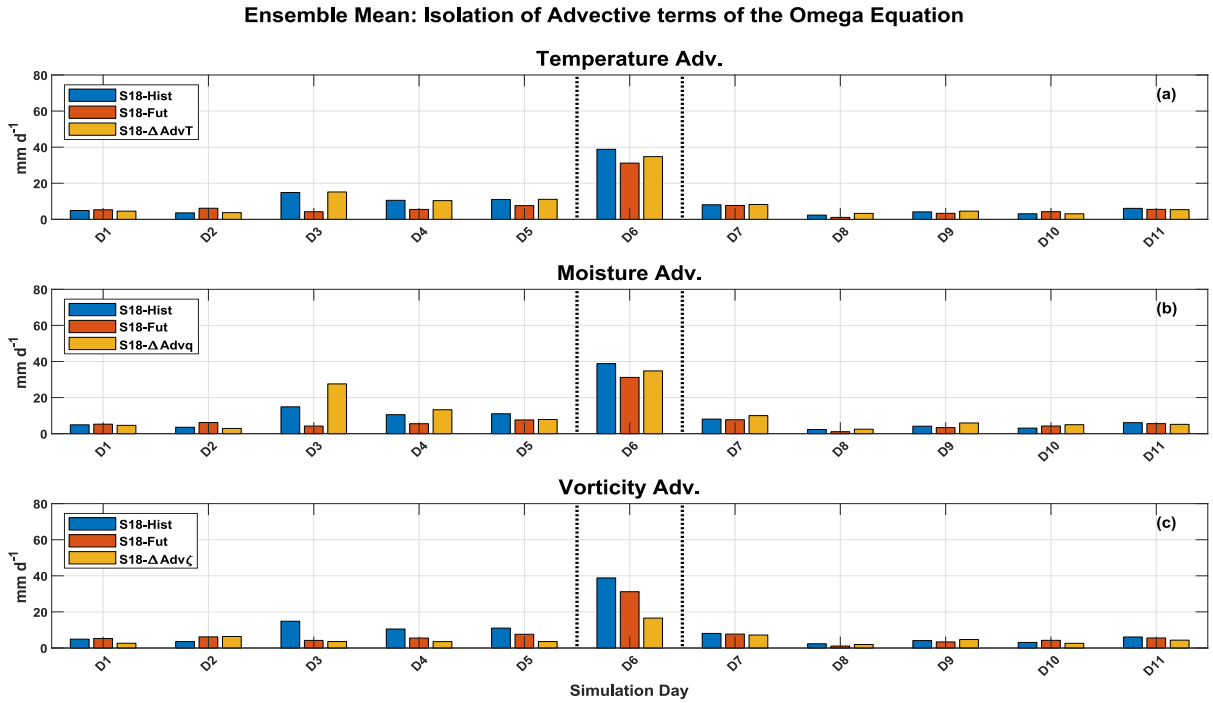

Figure 12: Same as figure 12. Exception: Location is S18.

Extreme precipitation associated with changes in temperature advection run is quantitatively comparable to the historical run in both figure 11 and 12. The changes visible in figure 12a are very small. It can be said based on these two figures that changes in temperature advection alone does not influence the decrease of extreme precipitation intensity in these locations. On the other hand, changes in moisture advection shows an increase in extreme precipitation intensity, figure 11b but an insignificant decrease in 12b. This increase may be linked to with Clausius-Clapeyron scaling (CC-scaling) through the thermodynamic component. CC-scaling relates an increase in surface temperature with an increase in the moisture holding capacity of a given atmospheric column (Trenberth, 1999; Trenberth et al., 2015), generally this can be associated with extreme precipitation increase. On a dynamical perspective an increase in moisture advection will result in more moisture being advected into the column thus increasing the overall moisture and that will have a positive effect on extreme precipitation intensity.

Changes in differential absolute vorticity advection alone captured the decrease in extreme precipitation intensity, figure 11c and 12c. Such results show an agreement with the initial sets of isolation runs. Zooming into the isolation of individual advective terms; it is seen that vorticity advection captures most of the decrease in extreme precipitation intensity. From this result we

can say that horizontal advections play a principal role on the decrease of extreme precipitation over the subtropical region. Furthermore, differential absolute vorticity advection is the key parameter associated with the decrease in extreme precipitation. Combining the advection runs (figure 8c and 9c) with the isolation of individual advective terms we may hypothesize that there is some nonlinear interaction taking place between temperature, moisture and vorticity advection.

3.5 Individual Omega Terms

Qualitative comparison was carried out to evaluate which term of the QGω contributes the most. The QGω was solved term-wise and vertical velocity associated with individual terms plotted. This is possible because the QGω is a linear equation; thus term-wise contributions can be solved individually. Taking omega to be zero at lower and upper boundaries, $\omega_B = \omega_{Top} = 0$. The ω can be decomposed:

$$\omega = \omega_\zeta + \omega_T + \omega_Q \tag{9}$$

ω_ζ is the vertical velocity component associated with vorticity advection only, ω_T is the vertical velocity component associated with temperature advection only and ω_Q is the vertical velocity component associated with diabatic heating only (Nie and Sobel 2016). Figure 13 below shows the vertical velocity associated with the total vorticity advection term, ω-Advζ. Figure 13a and c is vertical velocity associated with vorticity advection. Panel b and d is vertical velocity associated with temperature advection, ω-Adv$T$. This figure is mainly for case S27 case. It is interesting to note that ω-Advζ is an order of magnitude stronger that ω-Adv$T$. This contradicts Trenberth's (Bluestein, 1992) approach which showed that in given regions of the atmosphere there is a cancellation between ω-Advζ and ω-Adv$T$. In Trenberth's formulation, absolute vorticity is being advected by the thermal wind.

However, following Trenberth's reasoning this may be due to the region ($27°S, away\ from\ the\ extratropics$) that this analysis was done. Temperature advection term tends to be strong near frontal systems or jets streams (Bluestein, 1992; Holton and Hakim, 2012) Therefore, in this analysis it is expected that the temperature advection term be smaller than the absolute advection term.

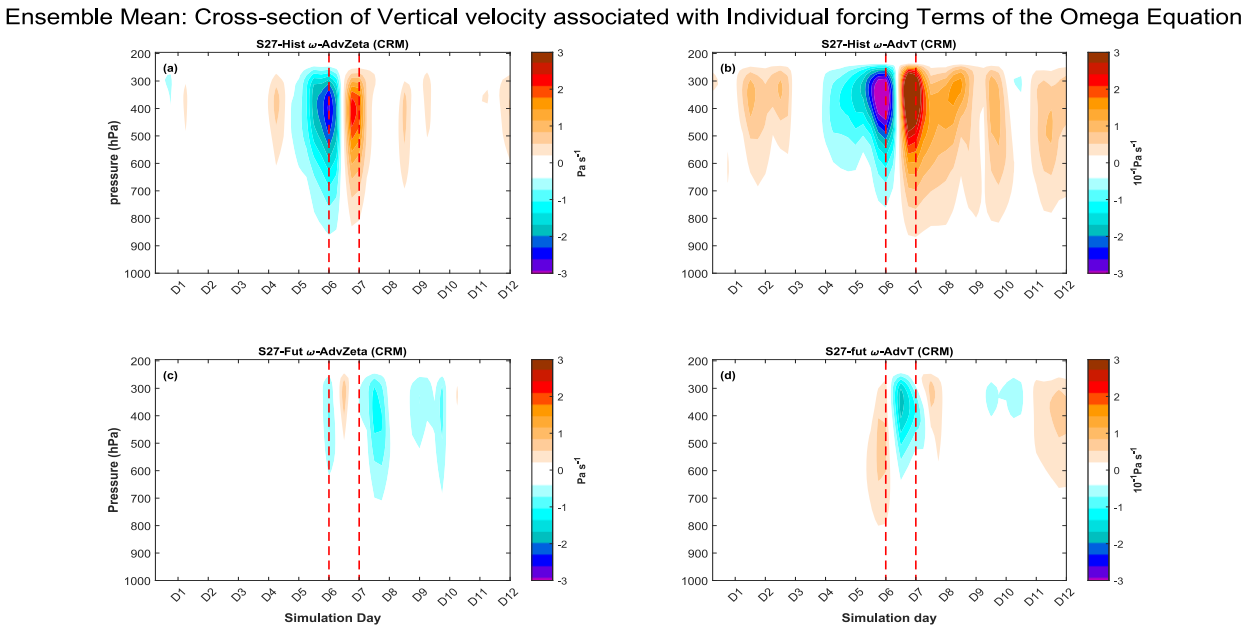

Figure 13: Comparison of vertical pressure velocity associated with individual terms of the QGω. (a) S27-Hist vertical velocity associated with vorticity advection, (b) S27-Fut vertical velocity associated with temperature advection. The values in panel (b) were multiplied by 10 for display purposes. (c) S27-Hist vertical velocity associated with vorticity advection. (d) S27-Fut vertical pressure velocity associated with temperature advection. The values in panel (d) were multiplied by 10 for display purposes. Red dotted line demarcates the extreme event

Since the QGω is linear, we can say that total vorticity advection term plays dominant role on the QGω. The relatively small contribution of the temperature advection can be associated with the nature of systems over this domain, near the tropics. The dipole that is seen on the first two panels is interesting since in panel c and d this structure is less pronounced. The shift in the cores of these term-wise velocities (panel d) may also explain the timing issues that were encountered with the CRM simulations.

3.6 Weakening of the circulation

Vertical velocity profiles are showing peak ascent between 700 and 500 hPa (figure 14). Figure 14d shows a weaker vertical velocity which is one order of magnitude lower than in figure 13a-c. Comparing the historical with future profiles there is evidence of weakening of vertical velocity strength. The weakening is associated with the changes in extreme precipitation intensity.

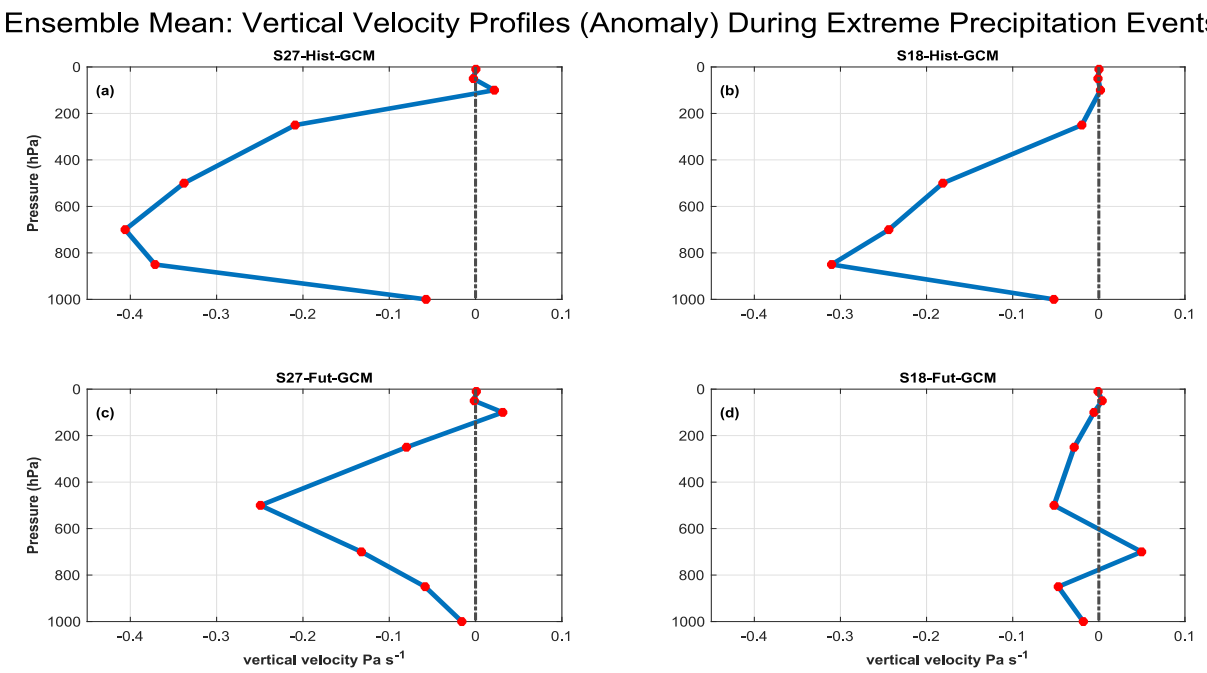

Figure 14: Daily mean domain-averaged vertical pressure velocity profiles on the day of extreme precipitation in the S27 case. (a) S27-Hist-GCM. (b) S18-His-GCM. (c) S27-Fut-GCM. (d) S27-Fut-GCM.

Further investigation at this level was performed to visualize the circulation pattern and structure in vertical pressure velocity and precipitation intensity. Figure 15 below compares precipitation and vertical velocity anomaly. Comparing figure 15 (a) and (b), the vertical velocity is in the same order of magnitude but relatively weaker in the future case (S27-Fut). Peak precipitation and vertical velocity are aligned in figure 15a. For the corresponding future case (figure 15b), there is no alignment between peak precipitation and vertical velocity. The strength of vertical velocity is relatively strong in figure 16a compared to figure 15b.

Figure 15a and b highlight the weakening of large-scale vertical velocity very well since both events here occurred in the same season, hence there is no seasonal effect in this change. Similar pattern is observed when comparing figure 15c and d. Peak precipitation is not aligned with peak vertical velocity. It is also interesting to see that vertical velocity in figure 15d is an order of magnitude smaller than in the other three figures. Therefore, what these figures are showing can be the influence of the circulation weakening within the regions that they are occurring. Examining figure 15 with table 1, it is worth noting that out of the 6 cases examined 4 are showing a seasonal shift whereby extreme precipitation occurs early into the season on the past climate but later into

the season on the future warmer climate. Such results are consistent with Brönnimann et al. (2018); Marelle et al. (2018).

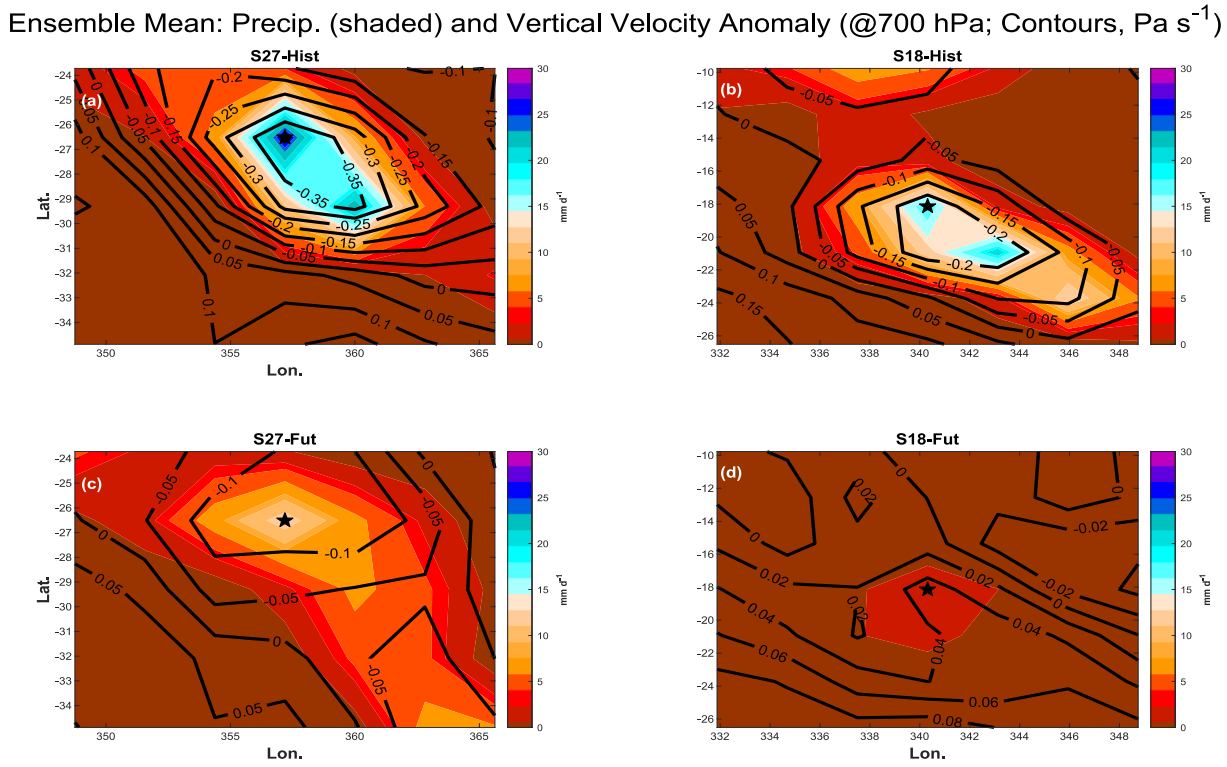

Figure 15: Comparison of 20-year maximum precipitation and ω_anomaly over the S27 region. (a) Extreme precipitation (shaded) and pressure velocity anomaly at 700 hPa (contours) from the CanESM2 historical during the extreme on the day of extreme precipitation. (b) Extreme precipitation (shaded) and pressure velocity anomaly at 700 hPa (contours) from the CanESM2 future at the day of extreme precipitation. The star indicates the location of the extreme precipitation event.

In summary, simulations were first performed over the ocean surfaces rather than land surfaces. Land surfaces are more physically complex compared to ocean surfaces. It was deemed prudent to start with the physically simpler S27 and S18 cases in order to develop our understanding of physical mechanisms as well as our technical comfort level with the CRM. There were also attempts to perform simulations over Alberta and other Canadian prairies where summertime extreme precipitation intensity is projected to decrease (Tandon et al., 2018b). However, there were technical challenges in maintaining the numerical stability of the CRM in this region. The challenges are due to the complicated effects of topographical uplift. Further investigation of extreme precipitation over land regions using our dynamical downscaling approach is being left for future work.

4. Chapter 4: Summary and conclusion

Dynamical downscaling experiments with a CRM were conducted to examine the dynamical mechanisms influencing projected changes of extreme precipitation intensity. The CRM reproduced a decrease in extreme precipitation intensity over the subtropical South Atlantic Ocean that was in line with CanESM2 projections. However, there was a case where the CRM did not capture the decrease in extreme precipitation. The CRM experiments showed that eddy length change and stability change are not principal contributors to projected decreases in extreme precipitation intensity. When applying changes in eddy length, some cases showed an increase while others showed a decrease precipitation intensity. Notable decrease in extreme precipitation associated with changes in eddy length occurred mostly at the location S18. Changes in horizontal advection accounted for most decrease in extreme precipitation intensity.

Investigating horizontal advection terms, temperature and moisture advection appeared to have a small contribution to the changes in extreme precipitation. Vorticity advection appeared to be playing a principal role in decrease of projected extreme precipitation. The comparison between ω-AdvT and ω-Advζ showed that ω-Advζ is the dominant term. In most cases ω-Advζ was 1-2 orders of magnitude larger than ω-AdvT. Overlaying vertical velocity anomaly and extreme precipitation and comparing between the 2 epochs showed a weakening in large scale vertical velocity. In the future epoch extreme precipitation peak was not coinciding with peak large-scale vertical velocity as it was the case with Historical epoch. Generally, there is a spatial shift in the distribution of extreme precipitation towards the south-east. The extreme events that examined occurred mostly in autumn and winter.

5. Chapter 5: Future Efforts

In the future it will be worth performing CRM experiments over land and during summer. Conducting these experiments in different climatological regions will also be a valuable task to undertake in the future. This will help test the sensitivity of this experiment and guide us to a clearer picture about the dynamical mechanisms influencing extreme precipitation intensity. The second effort will be to test the effect of parameterizing convection by using a single column model with convective parametrization. This will give important insights as convection is a vital part of many extreme precipitation events. Such knowledge will motivate future improvements of climate models and increase confidence in climate model projections. Such outcomes will benefit a range of stakeholders who require reliable regional projections of extreme precipitation to develop informed and effective adaptation and mitigation strategies in response to a changing climate. Events will also be selected in the same seasons to offset seasonality in our results. In future experiments cases will be selection strategically to have a separation between events dominated by large scale dry dynamics and convectively driven events. It will be interesting also to investigate perform a quantitative experiment looking at the shift in seasonality of extreme precipitation towards the cold season. Lastly investigating different time scales of extreme precipitation.

6. Bibliography

Ahmed, Vaqar, Amin Aslam Khan Malik, Shakeel Ramay, Zuhair Munawwar, and Amir Pervaiz. 2011. “National Economic and Environmental Development Study: The Case of Pakistan.” *Munich Personal RePEc Archive*.

American Meteorological Society. 2011. “American Meteorological Society Glossary of Meteorology.” Meteorology Glossary. 2011.

Arora, V. K., J. F. Scinocca, G. J. Boer, J. R. Christian, K. L. Denman, G. M. Flato, V. V. Kharin, W. G. Lee, and W. J. Merryfield. 2011. “Carbon Emission Limits Required to Satisfy Future Representative Concentration Pathways of Greenhouse Gases.” *Geophysical Research Letters* 38 (5): . https://doi.org/10.1029/2010GL046270.

Bao, Jiawei, Steven C. Sherwood, Maxime Colin, and Vishal Dixit. 2017. “The Robust Relationship Between Extreme Precipitation and Convective Organization in Idealized Numerical Modeling Simulations.” *Journal of Advances in Modeling Earth Systems* 9 (6). https://doi.org/10.1002/2017MS001125.

Barnes, Elizabeth A., and Dennis L. Hartmann. 2012. “The Global Distribution of Atmospheric Eddy Length Scales.” *Journal of Climate* 25 (9): 3409-16. https://doi.org/10.1175/JCLI-D-11-00331.1.

Bluestein, H. 1992. “Synoptic-Dynamic Meteorology in Midlatitudes, Vol. I: Principles of Kinematics and Dynamics.” *Oxford University Press, New York*.

Brönnimann, Stefan, Jan Rajczak, Erich Fischer, Christoph Raible, Marco Rohrer, and Christoph Schär. 2018. “Changing Seasonality of Moderate and Extreme Precipitation Events in the Alps.” *Natural Hazards and Earth System Sciences*. https://doi.org/10.5194/nhess-18-2047-2018.

David A. Randall, Richard A. Wood. 2007. “Climate Models and Their Evaluation.” *Evaluation*.

Davies, Huw C. 2015. “The Quasigeostrophic Omega Equation: Reappraisal, Refinements, and Relevance.” *Monthly Weather Review* 143 (1): 3–25. https://doi.org/10.1175/MWR-D-14-00098.1.

Dwyer, J. G., and P. A. O’Gorman. 2017. “Changing Duration and Spatial Extent of Midlatitude Precipitation Extremes across Different Climates.” *Geophysical Research Letters* 44 (11): 5863–71. https://doi.org/10.1002/2017GL072855.

Fischer, E. M., and R. Knutti. 2016. “Observed Heavy Precipitation Increase Confirms Theory and Early Models.” *Nature Climate Change*. Nature Publishing Group 6:98-991. https://doi.org/10.1038/nclimate3110.

Holton, James R., and Gregory J. Hakim. 2012. *An Introduction to Dynamic Meteorology: Fifth Edition*. *An Introduction to Dynamic Meteorology: Fifth Edition*. Vol. 9780123848. https://doi.org/10.1016/C2009-0-63394-8.

Hu, Yongyun, Han Huang, and Chen Zhou. 2018. “Widening and Weakening of the Hadley Circulation under Global Warming.” *Science Bulletin* 63 (10): 640-44. https://doi.org/10.1016/j.scib.2018.04.020.

Huffman, George J., Robert F. Adler, Philip Arkin, Alfred Chang, Ralph Ferraro, Arnold Gruber, John Janowiak, Alan McNab, Bruno Rudolf, and Udo Schneider. 1997. “The Global Precipitation Climatology Project (GPCP) Combined Precipitation Dataset.” *Bulletin of the American Meteorological Society* 78 (1): 5-20. https://doi.org/10.1175/1520-0477(1997)078<0005:TGPCPG>2.0.CO;2.

Ipcc. 2013. “Working Group I Contribution to the IPCC Fifth Assessment Report - Summary for Policymakers.” *Climate Change 2013: The Physical Science Basis*. https://doi.org/10.1017/CBO9781107415324.004.

Khairoutdinov, Marat F., and David A. Randall. 2003. “Cloud Resolving Modeling of the ARM Summer 1997 IOP: Model Formulation, Results, Uncertainties, and Sensitivities.” *Journal of the Atmospheric Sciences* 60 (4): 607–25. https://doi.org/10.1175/1520-0469(2003)060<0607:CRMOTA>2.0.CO;2.

Kidston, J., S. M. Dean, J. A. Renwick, and G. K. Vallis. 2010. “A Robust Increase in the Eddy Length Scale in the Simulation of Future Climates.” *Geophysical Research Letters* 37 (3): 1–4. https://doi.org/10.1029/2009GL041615.

Kronstadt, K. Alan, Pervaze A. Sheikh, and Bruce Vaughn. 2011. “Flooding in Pakistan: Overview and Issues for Congress.” *Environmental Stress in Pakistan and U.S. Interests*, 27–66.

Loriaux, Jessica M., Geert Lenderink, and A. Pier Siebesma. 2017. “Large-Scale Controls on Extreme Precipitation.” *Journal of Climate* 30 (3): 955-968. https://doi.org/10.1175/JCLI-D-16-0381.1.

Marelle, Louis, Gunnar Myhre, Øivind Hodnebrog, Jana Sillmann, and Bjørn Hallvard Samset. 2018. “The Changing Seasonality of Extreme Daily Precipitation.” *Geophysical Research Letters* 45 (20): 11352-60. https://doi.org/10.1029/2018GL079567.

Milrad, Shawn M., Kelly Lombardo, Eyad H. Atallah, and John R. Gyakum. 2017. “Numerical Simulations of the 2013 Alberta Flood: Dynamics, Thermodynamics, and the Role of Orography.” *Monthly Weather Review* 145 (8): 3049–72. https://doi.org/10.1175/MWR-D-16-0336.1.

Nie, Ji, and Adam H. Sobel. 2016. “Modeling the Interaction between Quasigeostrophic Vertical Motion and Convection in a Single Column.” *Journal of the Atmospheric Sciences* 73 (3): 1101–17. https://doi.org/10.1175/JAS-D-15-0205.1.

Nie, Ji, Adam H. Sobel, Daniel A. Shaevitz, and Shuguang Wang. 2018. “Dynamic Amplification of Extreme Precipitation Sensitivity.” *Proceedings of the National Academy of Sciences of the United States of America* 115 (38): 9467–72. https://doi.org/10.1073/pnas.1800357115.

O’Gorman, Paul A. 2015. “Precipitation Extremes Under Climate Change.” *Current Climate Change Reports* 1: 49-59. Springer. https://doi.org/10.1007/s40641-015-0009-3.

Pfahl, S., P. A. O’Gorman, and E. M. Fischer. 2017. “Understanding the Regional Pattern of Projected Future Changes in Extreme Precipitation.” *Nature Climate Change* 7 (6): 423–27. https://doi.org/10.1038/nclimate3287.

Pierce, David W., Tim P. Barnett, Benjamin D. Santer, and Peter J. Gleckler. 2009. “Selecting Global Climate Models for Regional Climate Change Studies.” *Proceedings of the National Academy of Sciences of the United States of America* 106 (21) 8441-8446. https://doi.org/10.1073/pnas.0900094106.

Rajczak, J., P. Pall, and C. Schär. 2013. “Projections of Extreme Precipitation Events in Regional Climate Simulations for Europe and the Alpine Region.” *Journal of Geophysical Research Atmospheres*. 118, 3610-3626. https://doi.org/10.1002/jgrd.502972013.

Riahi, Keywan, Shilpa Rao, Volker Krey, Cheolhung Cho, Vadim Chirkov, Guenther Fischer, Georg Kindermann, Nebojsa Nakicenovic, and Peter Rafaj. 2011. “RCP 8.5-A Scenario of Comparatively High Greenhouse Gas Emissions.” *Climatic Change* 109 (33). https://doi.org/10.1007/s10584-011-0149-y.

Tandon, Neil F., Ji Nie, and Xuebin Zhang. 2018. “Strong Influence of Eddy Length on Boreal

Summertime Extreme Precipitation Projections." *Geophysical Research Letters* 45 (10): 10665-72. https://doi.org/10.1029/2018GL079327.

Tandon, Neil F., Xuebin Zhang, and Adam H. Sobel. 2018a. "Understanding the Dynamics of Future Changes in Extreme Precipitation Intensity." *Geophysical Research Letters* 45 (6): 2870–78. https://doi.org/10.1002/2017GL076361.

Trenberth, Kevin E. 1999a. "Atmospheric Moisture Recycling: Role of Advection and Local Evaporation." *Journal of Climate* 12 (5 II): 1368–81. https://doi.org/10.1175/1520-0442(1999)012<1368:amrroa>2.0.co;2.

———. 1999b. "Conceptual Framework For Changes of Extremes of The Hydrological Cycle With Climate Change." *Climatic Change* 42: 327–39.

Trenberth, Kevin E., John T. Fasullo, and Theodore G. Shepherd. 2015. "Attribution of Climate Extreme Events." *Nature Climate Change* 5 (8): 725–30. https://doi.org/10.1038/nclimate2657.

Westra, Seth, Lisa V. Alexander, and Francis W. Zwiers. 2013. "Global Increasing Trends in Annual Maximum Daily Precipitation." *Journal of Climate* 26 (11): 3904–18. https://doi.org/10.1175/JCLI-D-12-00502.1.

WMO. 2018. "Guidelines on the Defintion and Monitoring of Extreme Weather and Climate Events." *Task Team on the Definition of Extreme Weather and Climate Events*. https://doi.org/10.1109/CSCI.2015.171.

Zheng, Feifei, Seth Westra, and Michael Leonard. 2015. "Opposing Local Precipitation Extremes." *Nature Climate Change* 5: 389-390. https://doi.org/10.1038/nclimate2579.